

Chapter II

Computer Simulation of Welding Processes

2.1 Introduction and Synopsis

Computer aided Design (*CAD*) and analysis and Computer Integrated Manufacturing (*CIM*) are popular topics for research. Computer aided drafting and engineering analysis such as Finite Element Method (*FEM*) are well developed. Finger & Dixon [1 and 2] categorize research areas in their review of theory and methodology of mechanical design. They agree that computer-based models provide the best opportunity to improve theories of design and increase their acceptance. Simulations are useful in designing the manufacturing process as well as the manufactured component itself.

Figure 2-1 shows an overview of some of the activities that will be performed during the product development cycle adopted from [3 and 4].

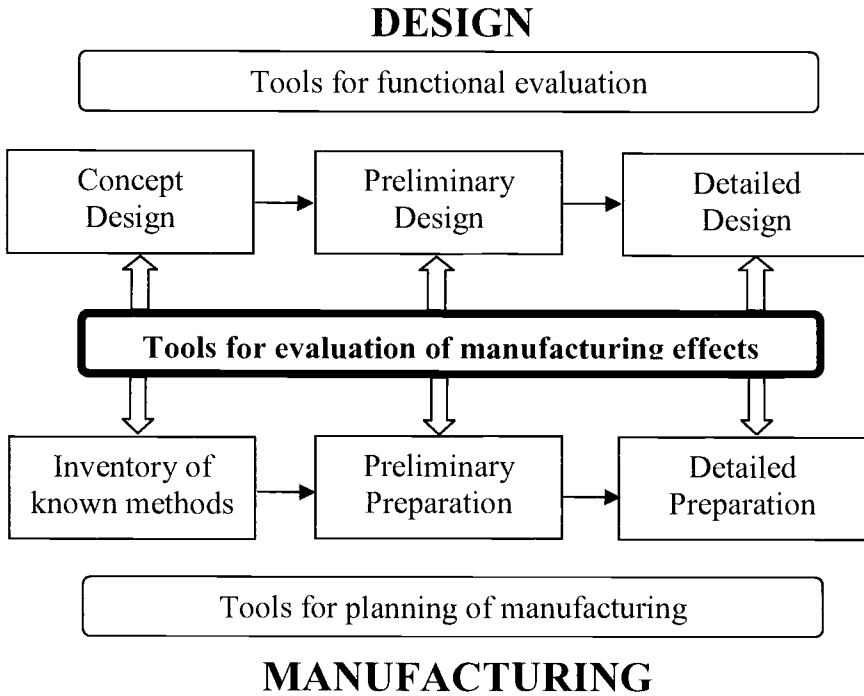


Figure 2-1: Tools for evaluation of manufacturing effects between functional evaluation and planning of manufacturing (vertical) also between concept and details (horizontal), from [3 and 4].

In Figure 2-1, the upper part presents the traditional tools for functional evaluation and the lower part show the systems for computer aided design and finite element programs. Design engineers will use these tools, especially to improve the product and its functionality as much as possible. Weld simulation belongs to the middle part which includes tools for evaluation of manufacturing effects. This covers the most negative effects of manufacturing, on the properties in different phases of the process leading to defects in material state, form accuracy, measurement tolerance, strength, hardness and other quality features. The development of tools dedicated to supporting the evaluation of manufacturing effects has lagged due to the complexity of simulation processes. In Figure 2-1 the lower part demonstrates the current tools for planning of

manufacturing, and above it, systems for programming robots and controlling material flow. Manufacturing engineers will use these tools especially to improve the production sequence and flow of material in the factory increasing the revenue of the manufactured product. Development steps from concept to detail in design and in manufacturing are shown in boxes. These steps must be run concurrently (simultaneous engineering), for which computing tools are inevitable requirements. Effort will be made in the entire process range, from raw material to the finished product, to include computers and simulations.

The calculation of weld simulation could not ignore computing tools in the future for innovative development of weld processes, weld design and their materials. Chihoski's [5] recommendation still says it best: "A changed set of conditions often changes the weld quality too subtly to be seen, except in large quantities, and there are too many possible changes to try. Hit or miss changes in the perfect lab (the production shop) are often not permitted. It would seem then to be of great use to the welding industry to develop and evolve computer programs that rigorously portray the stress and strain arrangements for different weld conditions. This route may be the only path from the current state of technology to the ideal in scientific promise, where a manufacturer who chooses an alloy and thickness and weld conditions can compute the value of each of the other weld conditions that minimize production problems".

2.2 The Computing Environment

2.2.1 Computational Geometry

In computer aided drafting, the computer stores the lines and symbols from the drawing, but does not understand them and cannot interpret them. With wire frame models that store vertices and edges, the computer has some understanding of the geometry and can rotate an object or at least its wire frame representation. However, the ambiguity of wire frames prevents the program from computing some values such as the volume of an object.

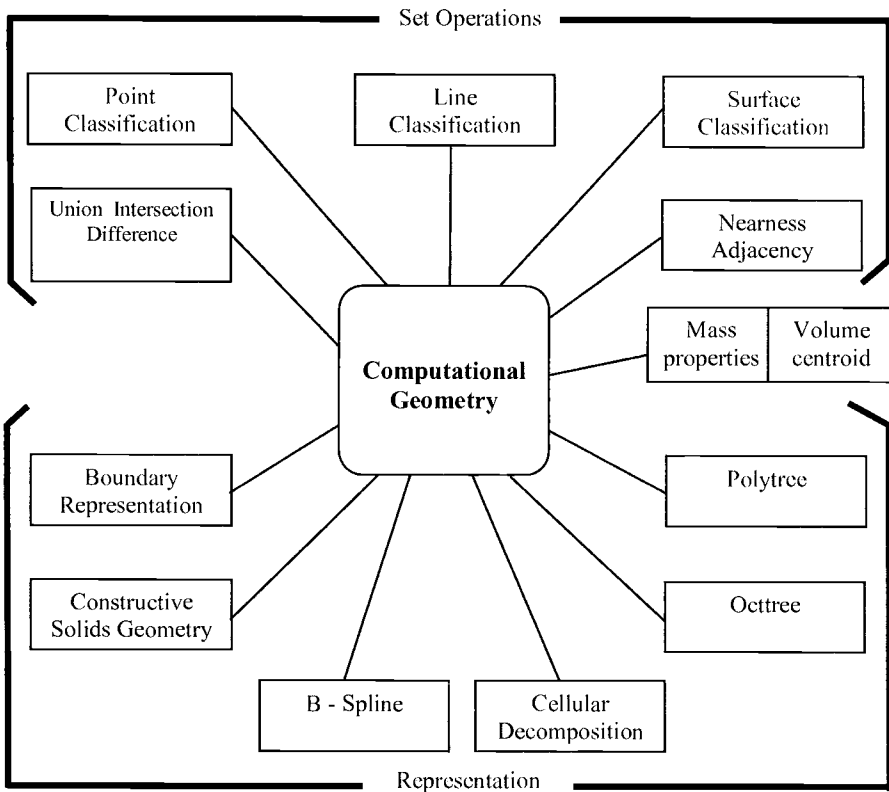


Figure 2-2: The representations and set operations that have been developed for computational geometry are shown above.

Modern computational geometry has developed representations and operations that overcome these difficulties, Figure 2-2. The best known of these is solids modeling which was developed to provide a mathematically complete representation of the geometry of an object [6].

Mathematicians usually approach geometry from one of two ways. Algebraic topology considers volume in $3D$ space, e. g., a cube. The boundary of the volume is an oriented surface or set of surfaces of zero thickness. The boundary a surface is a curve. The boundary of a curve is a point. Point set topology considers $3D$

space to filled with an infinite set of points. Each point is either inside, outside or on the boundary of a 3D object. An *FEM* mesh is best treated from the viewpoint of algebraic topology. In *FEM* analysis of temperature or stress, it is usual to take the viewpoint of point set topology.

Modeling is the process of preparing a computational model. To start creating the analytical model we first have to decide what kind of geometric approximation would be most suitable for our purpose. Figure 2-3 shows several alternatives of geometry.

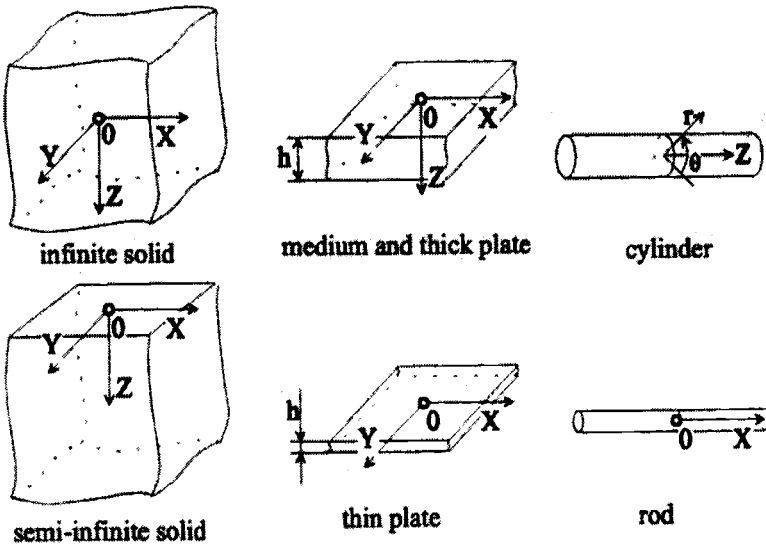


Figure 2-3: Different schemes of idealized body configuration, adopted from [18].

The next step towards analytical model creation is to choose the weld related approximation. Pilipenko [18] suggests the investigated problem can be classified by: time of action, mobility and dimensions. The time of action can be instantaneous or continuous and mobility, stationary or mobile. By the area of distribution, it can be presented as a point (dim=0), line (dim=1), plane (dim=2) and volume (dim=3).

To get a general view, all the classifications are presented in the

scheme on Figure 2-4.

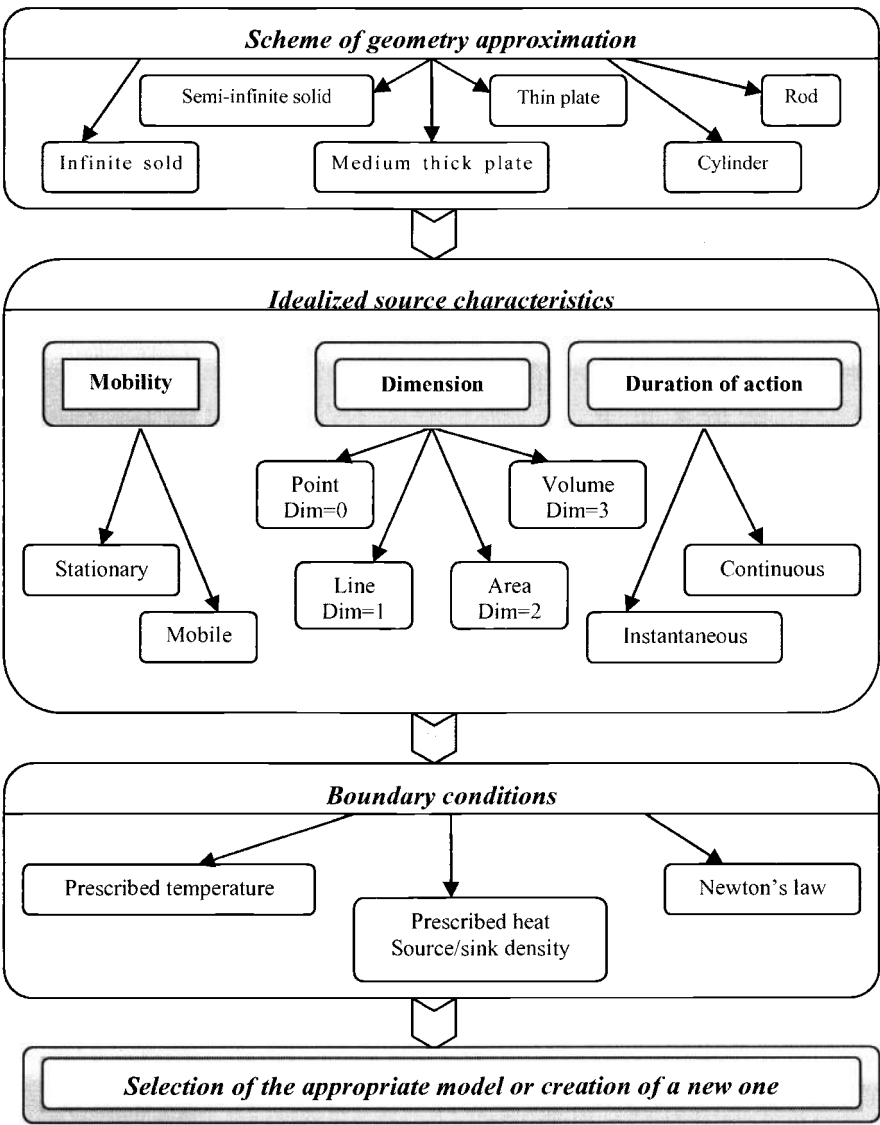


Figure 2-4: Flow chart of the model selection process, from [18].

At present many different analytical models are known. Lindgren presents a review of several in [22]. The earliest numerical predictions of residual stresses were probably those of Tall [21], Vinokurov [76] and Okerblom [75]. Tsuji [23] performed similar calculations. The mechanical analysis was essentially one-dimensional, although the analytic solution for the temperatures was two dimensional in the work by Tall. The earliest two-dimensional finite element analysis appeared in the early 1970s, by Iwaki and Masubuchi [24], Ueda and Yamakawa [25, 26 and 27], Fujita et al. [28], Hibbitt and Marcal [29] and Friedman [30]. The early simulations by Fujita et al. [31] and Fujita and Nomoto [32] used only a thermo elastic material model. Although in welding the reality is 3D and transient, and 3D analysis is the most general formulation, to minimize computing costs many analysts have used lower dimensional models. However, they have long sought to perform full 3D analysis of welds. The first analyses of this kind were reported in 1986 [33-35].

2.2.2 Models for Welding Heat Sources

Theoretical Formulations

The basic theory of heat flow that was developed by Fourier and applied to moving heat sources by Rosenthal [38] and Rykalin [37] in the late 1930s is still the most popular analytical method for calculating the thermal history of welds. As many researchers have shown, Rosenthal's point or line heat source models are subject to a serious error for temperatures in or near the fusion zone (*FZ*) and heat affected zone (*HAZ*). The infinite temperature at the heat source assumed in this model and the temperature sensitivity of the material thermal properties increases the error as the heat source is approached. The effect of these assumptions and others on the accuracy of temperature distributions from the Rosenthal analysis has been discussed in detail by Myers et al. [39].

To overcome most of these limitations several authors have used the finite element method (*FEM*) to analyze heat flow in welds. Since Rosenthal's point or line models assume that the flux and

temperature is infinite at the source, the temperature distribution has many similarities to the stress distribution around the crack tip in linear elastic fracture mechanics. Therefore many of the *FEM* techniques developed for fracture mechanics can be adapted to the Rosenthal model. Certainly it would be possible to use singular *FEM* elements to analyze Rosenthal's formulation for arbitrary geometries. This would retain most of the limitations of Rosenthal's analysis but would permit complex geometries to be analyzed easily. However, since it would not account for the actual distribution of the heat in the arc and hence would not accurately predict temperatures near the arc, this approach is not pursued here. Pavelic et al. [40] first suggested that the heat source should be distributed and he proposed a Gaussian distribution of flux deposited on the surface of the workpiece. Figure 2-5 represents a circle surface heat source and a hemispherical volume source, both with Gaussian normal distribution (bell shape curves), in a mid-thick plate. The geometrical parameters of heat flux distribution are estimated from the results of weld experiments (molten zone, size and shape and also temperature cycle close to molten zone).

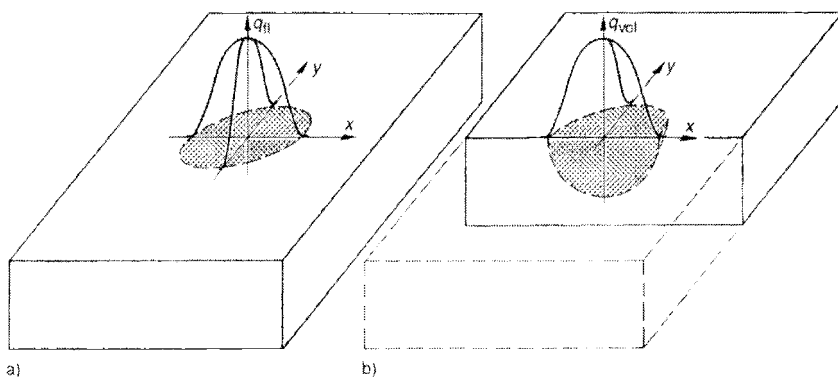


Figure 2-5 Heat source distribution in weldment: circular form surface source (a) and hemispherical volume source (b); Gaussian distribution of the surface related source density q_{fl} and volume related source density q_{vol} [3].

The subsequent works of Andersson [41], Krutz and Segerlind [42] and Friedman [43] are particularly notable. In References [42] and [43] Pavelic's 'disc' model is combined with *FEM* analysis to

achieve significantly better temperature distributions in the fusion and heat affected zones than those computed with the Rosenthal model.

While Pavelic's 'disc' model is certainly a significant step forward, some authors have suggested that the heat should be distributed throughout the molten zone to reflect more accurately the digging action of the arc. This approach was followed by Paley [44] and Westby [45] who used a constant power density distribution in the fusion zone (FZ) with a finite difference analysis, but no criteria for estimating the length of the molten pool was offered. In addition, it is difficult to accommodate the complex geometry of real weld pools with the finite difference method.

The analyst requires a heat source model that accurately predicts the temperature field in the weldment. A non-axisymmetric three-dimensional heat source model which is proposed in this book achieves

this goal. It is argued on the basis of molten zone observations that this is a more realistic model and more flexible than any other model yet proposed for weld heat sources. Both shallow and deep penetration welds can be accommodated as well as asymmetrical situations.

The proposed three-dimensional 'double ellipsoid' configuration heat source model is the most popular form of this class of heat source models [46]. It is shown that the 'disc' of Pavelic et al [40] and the volume source of Paley and Hibbert [44] and Westby [45] are special cases of this model. In order to present and justify the double ellipsoid model, a brief description of the Pavelic 'disc' and of the Friedman [43] modification for *FEM* analysis is necessary. In addition, the mathematics of the disc is extended to spherical, ellipsoidal and finally to the double ellipsoidal configuration. Finally, it is pointed out the most general form of this class of model has a general heat source distribution function.

Model Considerations

The interaction of a heat source (arc, electron beam or laser) with a weld pool is a complex physical phenomenon that still cannot be

modeled rigorously. It is known that the distribution of pressure and shear from the arc source, droplets from the electrode the effects of surface tension, buoyancy forces and molten metal viscosity combine to cause weld puddle distortion and considerable stirring. Because of the arc 'digging' and stirring, it is clear that the heat input is effectively distributed throughout a volume in the workpiece.

The 'disc' model is more realistic than the point source because it distributes the heat input over a source area. In fact, for a preheat torch that causes no melting this may be a very accurate model indeed. However, in the absence of modeling the weld pool free boundary position, the applied tractions, and convective and radiative conditions between the weld pool and the arc, some form of idealization of the heat source is necessary to achieve as good an approximate solution as one can afford. The disc model does not account for the rapid transfer of heat throughout the fusion zone *FZ*. In particular, it is not possible to predict the deep penetration *FZ* of an electron beam *EB* or laser weld with the surface disc model. A comparison of calculated thermal history data (disc model) with measured values during author's investigations [46] underscored the need for an 'effective volume source' such as the one suggested by Paley and Hibbert [44]. In addition, it was found necessary to generate a volume source with considerable flexibility, i.e., the double ellipsoid model. With less general shapes such as a hemisphere or a single ellipsoid significant discrepancies between the computed and measured temperature distributions could not be resolved.

The size and shape of the 'double ellipsoid' i.e., the semi-axes lengths, can be fixed by recognizing that the solid-liquid interface is the melting point isotherm. In reality the melting point is a function of curvature and the speed of the liquid-solid interface but the changes have been ignored in most models published to date. At the same time weld pool temperature measurements have shown that the peak temperature in the weld pool is often 300 to 500 °C above the melting point. The accuracy with which the heat source model predicts the size and shape of the *FZ* and the peak temperatures is probably the most stringent test of the performance of the model. In

the author's investigation [46] it was found that the most accuracy was obtained when the ellipsoid size and shape were equal to that of the weld pool. The non-dimensional system suggested by Christensen [48] can be used to estimate the ellipsoid parameters. Furthermore a Gaussian distribution is assumed centered at the origin of the heat source.

Gaussian Surface Flux Distribution

In the 'circular disc' model proposed by Pavelic et al [40], the thermal flux has a Gaussian or normal distribution in the plane, Figure 2-6:

$$q(r) = q(0)e^{-Cr^2} \quad (2-1)$$

where:

$q(r)$ = Surface flux at radius r (W/m^2)

$q(0)$ = maximum flux at the center of the heat source (W/m^2)

C = distribution width coefficient (m^{-2})

r = radial distance from the center of the heat source (m)

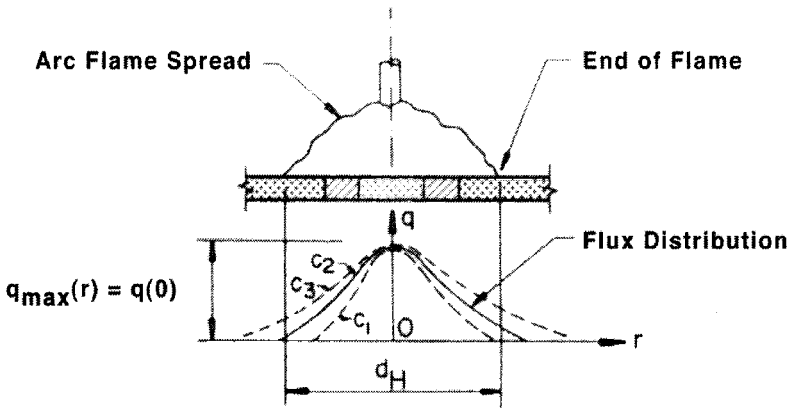


Figure 2-6: Circular disc heat source [40]

A simple physical meaning can be associated with C . If a uniform flux of magnitude $q(0)$ is distributed in a circular disk of diameter $d = 2/\sqrt{C}$, the rate of energy input would be ηIV , i.e., the

circle would receive all of the energy directly from the arc. Therefore the coefficient, C , is related to the source width; a more concentrated source would have a smaller diameter d and a larger value of C . To translate these concepts into practice, the process model for the normal distribution circular surface of the heat flux for laser beam welding and submerged arc welding, is illustrated in Figure 2-7.

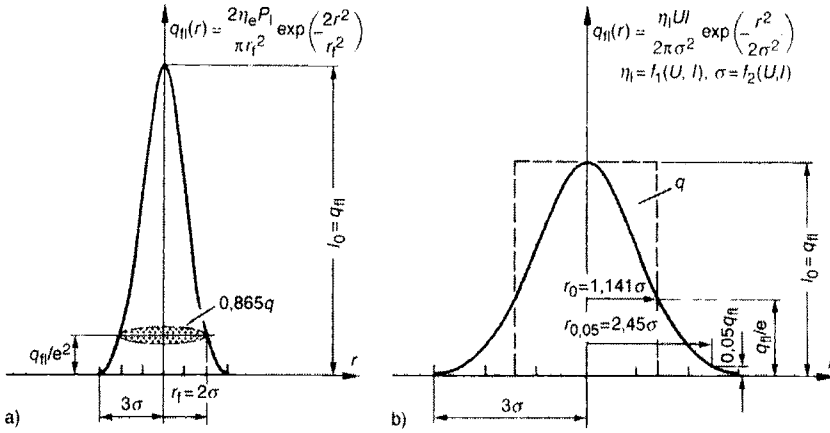


Figure 2-7: Normal distribution circular surface heat source and related parameters (radial distance from center σ) by laser beam welding (a) and by submerged arc welding (b); with laser efficiency coefficient η_e , the laser power P_I , the focus diameter $2r_f$, the arc efficiency coefficient η_I , voltage of arc V , the current I , the maximum flux at the center of the heat source $q(0)$ equal intensity I_0 , Euler number $e=2,71828\dots$; from Sudnik (unpublished) and Radaj [3].

The curve of the submerged arc welding is wide and low and the curve of the laser beam welding is in contrast, narrow and high. The laser beam has high intensity and a small diameter. The laser power P_I on the surface of the workpiece considering the efficiency coefficient is used as heat flux (power) q and/or heat power density q_{II} . The circular normal distribution is described by the focus radius $r_f = 2\sigma$ which contains 86% of the heat power.

The arc welding has less intensity and larger diameter. The arc power VI on the surface of the workpiece considering the arc efficiency coefficient is used as heat flux q and/or heat power

density q_{η} . For the circular normal distribution two different descriptions are used. The source radius $r_{0.05}$, in this heat power density is reduced by 5% (Rykalin [37] or the source radius r_0 of a same power source with constant heat power density (Ohji et al [51, 73]). The particular problem which exists for the definition of the heat source in arc welding is that both the arc efficiency η_I and the radial distance from the center σ are functions of the voltage V and the current I of the arc (Sudnik and Erofeew [72]).

The effective radius r_0 and/or $r_{0.05}$ of the circular surface heat source are derived from the maximum surface width of the molten zone. The heat flow density from the surface $q_{\eta}(x, y)$ for known r_0 and/or $r_{0.05}$ is defined from the power data of the weld heat source, considering the heat transfer efficiency. This is shown in Figure 2-7 for the laser beam welding and arc welding. If weld metal is added the related heat should be considered.

Experiments have shown that a significant amount of heat is transferred by radiation and convection from the arc directly to the solid metal without passing through the molten pool. Based on this observation, Pavelic et al. [40] developed a correlation showing the amount and the distribution of this heat over the solid material. In their study, provisions were made for convective and radiative losses from the heated plate to the surroundings as well as variable material properties.

Friedman [43] and Krutz and Segerland [42] suggested an alternative form for the Pavelic 'disc'. Expressed in a coordinate system that moves with the heat source as shown in Figure 2-8, Eq. (2-2) takes the form:

$$q(x, \xi) = \frac{3Q}{\pi c^2} e^{-3x^2/c^2} e^{-3\xi^2/c^2} \quad (2-2)$$

where:

Q = energy input rate (W)

c = is the characteristic radius of heat flux distribution (m)

It is convenient to introduce an (x, y, z) coordinate system fixed in the workpiece. In addition, a lag factor τ is needed to define the position of the source at time $t = 0$, Figure 2-8.

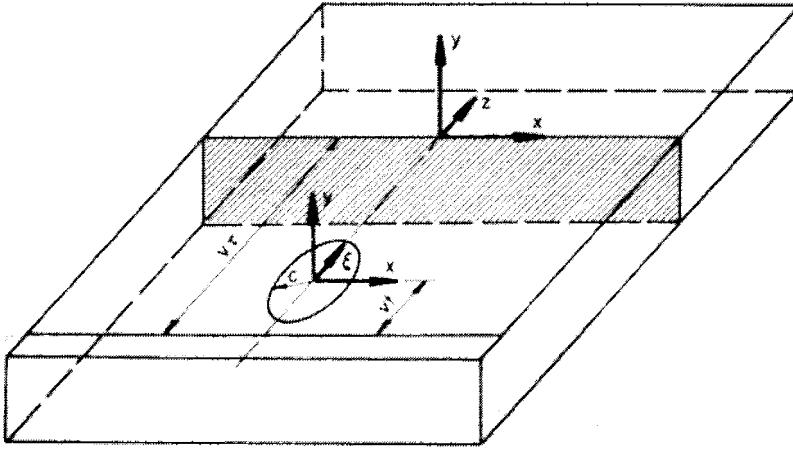


Figure 2-8: Coordinate system used for the FEM analysis of disc model according to Krutz and Segerlind [42]

The transformation relating the fixed (x, y, z) and moving coordinate system (x, y, ξ) is:

$$\xi = z + v(\tau - t) \quad (2-3)$$

where v is the welding speed (m/s). In the (x, y, z) coordinate system Eq. (2-2) takes the form:

$$q(x, z, t) = \frac{3Q}{\pi c^2} e^{-3x^2/c^2} e^{-3[z + v(\tau - t)]^2/c^2} \quad (2-4)$$

For $x^2 + \xi^2 < c^2$. For $x^2 + \xi^2 > c^2$, $q(x, \xi, t) = 0$

To avoid the cost of a full three-dimensional *FEM* analysis some authors assume negligible heat flow in the longitudinal direction; i.e., $\partial T / \partial z = 0$. Hence, heat flow is restricted to an x - y plane, usually positioned at $z = 0$. This has been shown to cause little error except for low speed high heat input welds [41]. The disc moves along the surface of the workpiece in the z direction and deposits heat on the reference plane as it crosses. The heat then diffuses outward (x - y direction) until the weld cools.

Hemi-spherical Power Density Distribution

For welding situations, where the effective depth of penetration is small, the surface heat source model of Pavelic, Friedman and Krutz has been quite successful. However, for high power density sources such as the laser or electron beam, it ignores the digging action of the arc that transports heat well below the surface of the weld pool. In such cases a hemispherical Gaussian distribution of power density (W/m^3) would be a step toward a more realistic model. The power density distribution for a hemispherical volume source can be written as:

$$q(x, y, \xi) = \frac{6\sqrt{3}Q}{c^3 \pi \sqrt{\pi}} e^{-3x^2/c^2} e^{-3y^2/c^2} e^{-3\xi^2/c^2} \quad (2-5)$$

where $q(x, y, \xi)$ is the power density (W/m^3). Eq. (2-5) is a special case of the more general ellipsoidal formulation developed in the next section.

Though the hemispherical heat source is expected to model an arc weld better than a disc source, it, too, has limitations. The molten pool in many welds is often far from spherical. Also, a hemispherical source is not appropriate for welds that are not spherically symmetric such as a strip electrode, deep penetration electron beam, or laser beam welds. In order to relax these constraints, and make the formulation more accurate, an ellipsoidal volume source has been proposed.

Ellipsoidal Power Density Distribution

The Gaussian distribution of the power density in an ellipsoid with center at $(0, 0, 0)$ and semi-axis a, b, c parallel to coordinate axes x, y, ξ can be written as:

$$q(x, y, \xi) = q(0) e^{-Ax^2} e^{-By^2} e^{-C\xi^2} \quad (2-6)$$

where $q(0)$ is the maximum value of the power density at the center of the ellipsoid.

Conservation of energy requires that:

$$2Q = 2\eta VI = 8 \int_0^\xi \int_0^y \int_0^x q(0) e^{-Ax^2} e^{-By^2} e^{-C\xi^2} dx dy d\xi \quad (2-7)$$

where;

η = Heat source efficiency

V = voltage

I = current

Evaluation of Eq. (2-7) produces the following:

$$2Q = \frac{q(0)\pi\sqrt{\pi}}{\sqrt{ABC}} \quad (2-8)$$

$$q(0) = \frac{2Q\sqrt{ABC}}{\pi\sqrt{\pi}} \quad (2-9)$$

To evaluate the constants, A , B , C , the semi-axes of the ellipsoid a , b , c in the directions x , y , ξ are defined such that the power density falls to $0.05 q(0)$ at the surface of the ellipsoid. In the x direction:

$$q(a, 0, 0) = q(0) e^{-Aa^2} = 0.05 q(0) \quad (2-10)$$

Hence

$$A = \frac{\ln 20}{a^2} \approx \frac{3}{a^2} \quad (2-11)$$

Similarly

$$B \approx \frac{3}{b^2} \quad (2-12)$$

$$C \approx \frac{3}{c^2} \quad (2-13)$$

Substituting A , B , C from Eqs. (2-11) to (2-13) and $q(0)$ from Eq. (2-9) into Eq. (2-6):

$$q(x, y, \xi) = \frac{6\sqrt{3}Q}{abc\pi\sqrt{\pi}} e^{-3x^2/a^2} e^{-3y^2/b^2} e^{-3\xi^2/c^2} \quad (2-14)$$

The coordinate transformation, Eq. (2-3), Figure 2-8, can be substituted into Eq. (2-14) to provide an expression for the ellipsoid in the fixed coordinate system.

$$q(x, y, z, t) = \frac{6\sqrt{3}Q}{abc\pi\sqrt{\pi}} e^{-3x^2/a^2} e^{-3y^2/b^2} e^{-3[z+v(\tau-t)]^2/c^2} \quad (2-15)$$

If heat flow in the z direction is neglected, an analysis can be performed on the z - y plane located at $z = 0$ which is similar to the 'disc' source. The power density is calculated for each time increment, where the ellipsoidal source intersects this plane.

Double Ellipsoidal Power Density Distribution

Calculation experience with the ellipsoidal heat source model revealed that the temperature gradient in front of the heat source was not as steep as expected and the gentler gradient at the trailing edge of the molten pool was steeper than experimental measurements. To overcome this limitation, two ellipsoidal sources were combined as shown in Figure 2-9. The front half of the source is the quadrant of one ellipsoidal source, and the rear half is the quadrant of another ellipsoid. The power density distribution along the ξ axis is shown in Figure 2-9.

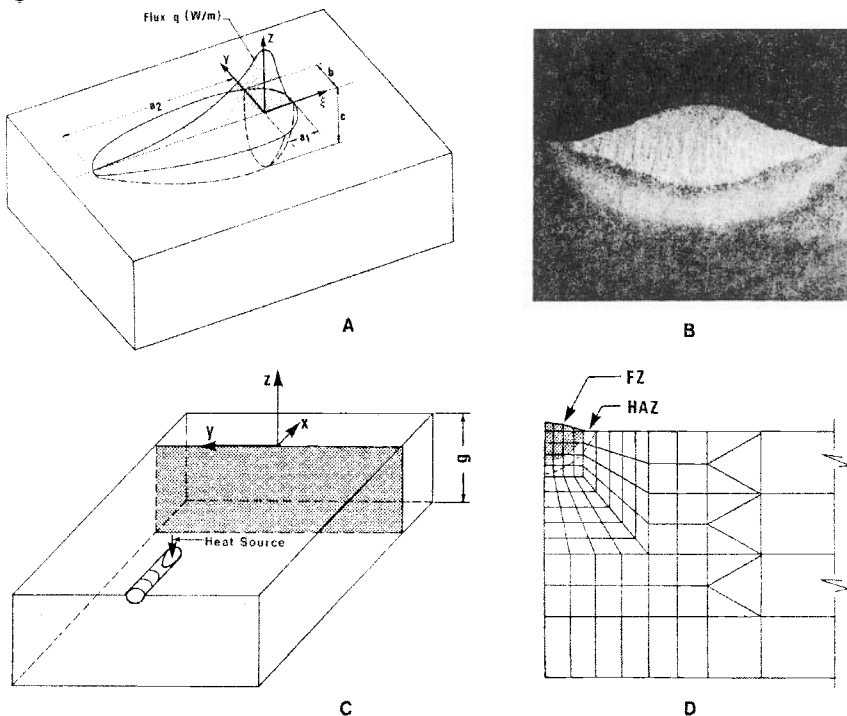


Figure 2-9: Double ellipsoid heat source configuration together with the power distribution function along the ξ axis (A), Cross-section of an SMAW weld bead

on a thick plate low carbon steel ($V=30$ volts, $I=265$ amps, $v=3.8$ mm/s, $g=38$ mm, $T_0=20.5$ °C), Reference plane concept and mesh used for the analysis will be discussed in the following chapters (D).

In this model, the fractions f_f and f_r of the heat deposited in the front and rear quadrants are needed, where $f_f + f_r = 2$. The power density distribution inside the front quadrant becomes:

$$q(x, y, z, t) = \frac{6\sqrt{3}f_f Q}{abc\pi\sqrt{\pi}} e^{-3x^2/a^2} e^{-3y^2/b^2} e^{-3[z+v(\tau-t)]^2/c^2} \quad (2-16)$$

Similarly, for the rear quadrant of the source the power density distribution inside the ellipsoid becomes:

$$q(x, y, z, t) = \frac{6\sqrt{3}f_r Q}{abc\pi\sqrt{\pi}} e^{-3x^2/a^2} e^{-3y^2/b^2} e^{-3[z+v(\tau-t)]^2/c^2} \quad (2-17)$$

In Eqs. (2-16) and (2-17), the parameters a , b , c can have different values in the front and rear quadrants since they are independent. Indeed, in welding dissimilar metals, it may be necessary to use four octants, each with independent values of a , b and c .

In cases where the fusion zone differs from an ellipsoidal shape, other models should be used for the flux and power density distribution. For example, in welds with a cross-section shaped as shown in Figure 2-10, four ellipsoid quadrants can be superimposed to more accurately model such welds.

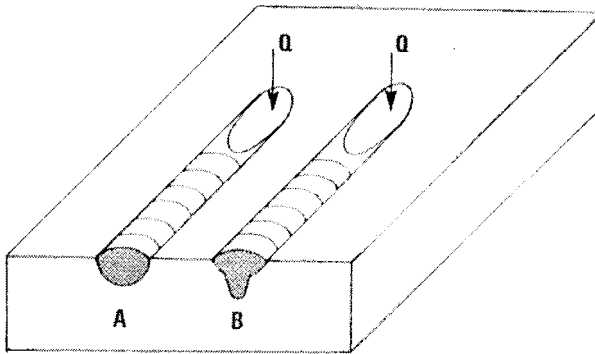


Figure 2-10: Cross-sectional weld shape of the fusion zone where a double ellipsoid is used to approximate the heat source (A), compound double ellipsoids must be superimposed to more accurately model such welds.

For deep penetration electron and laser beam welds, a conical distribution of power density which has a Gaussian distribution radially and a linear distribution axially has yielded more accurate results, Figure 2-11.

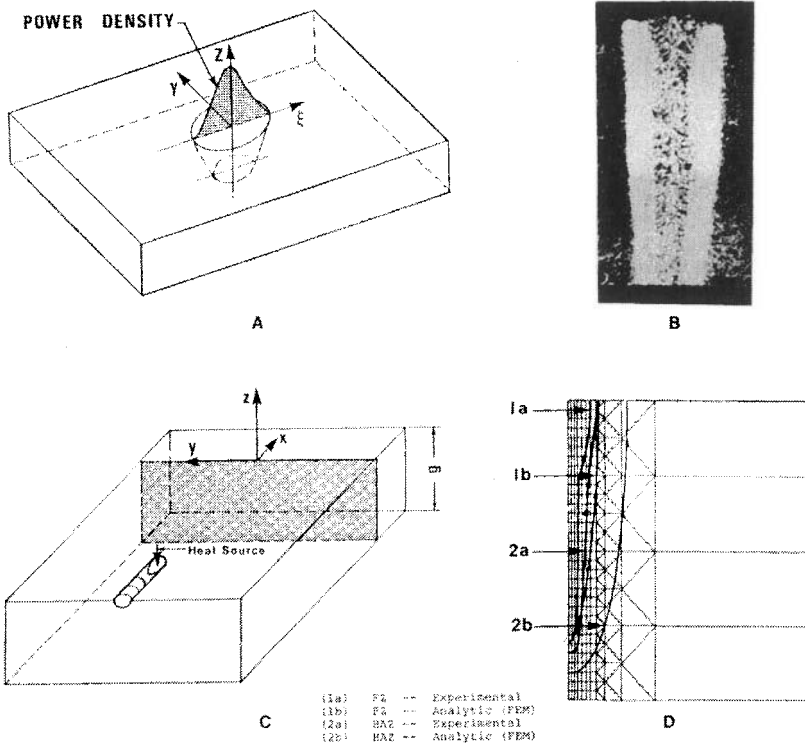


Figure 2-11: A conical weld heat source used for analyzing deep penetration electron beam or laser welds; conical source (A), typical electron beam weld (B), cross-sectional kinematic model with reference plane (C) and computed and measured Fusion zone (FZ) and heat affected zone (HAZ) boundaries, ($V=70$ kV, $I=40$ mA, $v=4.23$ mm/s, $g=12.7$ mm and $T_0=21^\circ\text{C}$).

The analyst must specify these functions or at least the parameters such as weld current, voltage, speed, arc efficiency and the size and position of the discs, ellipsoids and/or cones. In some cases the weld pool size and shape can be estimated from cross-sectional metallographic data and from weld pool surface ripple markings. If such data are not available, the method for estimating the weld pool dimensions suggested by Christensen [48] for arc

welds and by Bibby et al [68] for deep penetration electron beam or laser welds should be used.

The size and shape of the heat source model is fixed by the ellipsoid parameters defined in Figure 2-10. Good agreement between actual and computed weld pool size is obtained if the size selected is about 10% smaller than the actual weld pool size. If the ellipsoid semi-axes are too long then the peak temperature is too low and the fusion zone too small. The author's experience is that accurate results are obtained when the computed weld pool dimensions are slightly larger than the ellipsoid dimensions. This is easily achieved in a few iterations. Chakravarti et al [69] have studied the sensitivity of the temperature field to the ellipsoid parameters.

On the one hand these distribution functions can be criticized as "fudge" factors. On the other hand, they do enable accurate temperature fields to be computed. Chosen wisely, varying any parameter changes the computed temperature field. It can be argued that they are needed to model the many complex effects that are quantitatively known, such as electrode angle, arc length, joint design and shielding gas composition [70].

2.2.3 Kinematic Models for Welding Heat Transfer

Having selected a model for the heat source, the analyst has the option of assuming that the heat flows only in cross-sectional planes, only in the plane of the plate, only in a radial direction or is free to flow in all three dimensions, Figure 2-12. Such assumptions are analogous to those applied to the displacement field in beams, plates and shells in structural analysis. Since assumptions restrict the orientation of the thermal gradient, it is suggested they be called kinematic models. Of course, these kinematic models are quite distinct from the heat source models described in the previous section. These three models are discussed in detail in [36].

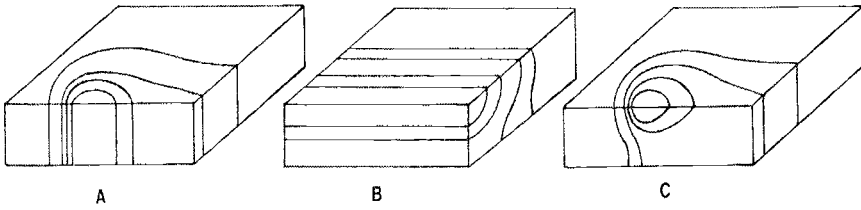


Figure 2-12: By constraining the thermal flux and hence the temperature gradients, the kinematic models are consistent with the temperature fields shown in; (A) in-plane, (B) cross-sectional models and (C) 3D models imply temperature.

The most popular has been the cross-sectional model which assumes that heat flow in the direction of welding is zero. This is surprisingly a subtle model. Strictly, it is limited to steady state analysis of prismatic geometries with the weld parallel to the prismatic axis. How can such a model possibly be accurate since some heat clearly must flow in the direction of welding? The answer is that the heat input has been modified to account for the heat that flows in the longitudinal direction. Because it uses relatively few *2D* elements, it is computationally one of the cheapest models.

The next most popular kinematic model has been the in-plane model. It assumes the heat flow normal to the weld plate is zero. The advantage of the in-plane over the cross-sectional model is its capability for computing the starting and ending transients. However, because it tends to require rather more elements and more time steps, the computational costs are higher [19]. It has not been used extensively.

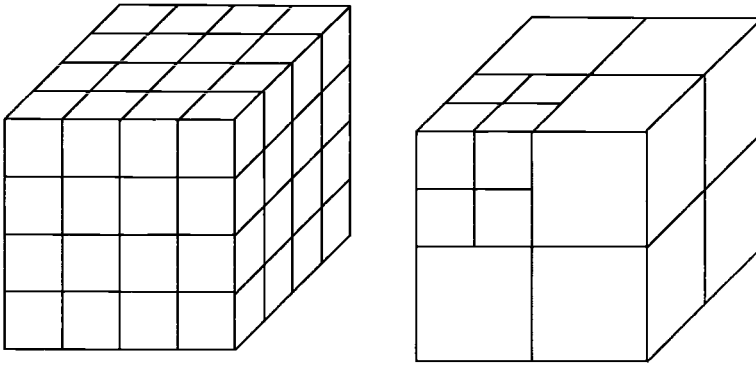
In choosing a kinematic model, the analyst must balance accuracy against cost. In all cases, reality is three dimensional but the cost of analysis is the highest. Constraining heat flow to the plane of the plate can achieve useful accuracy for thin plates, particularly with deep penetration plasma, electron and laser beam welds. Assuming heat flows only in the cross-sectional plane can provide a useful and economical approximation for many welding situations. If the thermal diffusivity is sufficiently low and welding speed sufficiently high, this can be an accurate model. In particular, the results from a low cost cross-sectional analysis can be helpful in designing an efficient *3D* mesh.

The thermal shell model is a generalization of the in-plane model to curved surfaces. It assumes that no heat flows normal to the surface and that all heat flows in the tangent plane, i.e., the temperature gradient lies in the tangent plane. Where conditions hold to an adequate accuracy, the shell model has several advantages. The shell element usually has half the number of degrees of freedom and half the bandwidth, which reduces the computing costs. Even more important, it allows larger elements than the equivalent 3D elements because they are better conditioned numerically.

In 3D analyses the kinematic model is obviously correct. The issue is to reduce the computational cost to acceptable levels for meshes that achieve useful accuracy. The principal tools are optimizing the mesh and creating efficient solvers.

In 3D analysis, brick elements are preferred because they tend to be more accurate and easier to use and interpret than tetrahedral elements. However, it is more difficult to grade a mesh with small brick elements near the welding arc to capture the rapid changes in temperature and with large brick elements far from the arc where the temperature varies slowly.

To solve these problems McDill et al. [10 and 47] developed a special brick element for graded 3D meshes. The grading elements of McDill have made a major contribution in optimizing the mesh for the analysis of welds. These elements reduce the computational complexity from $O(n^7)$ for a cube with uniform mesh with n elements on an edge to $O(\log_2 n)$ for the cube with a graded mesh. In both cases, the problem has a point load on one corner of the cube and direct solvers are used. In this problem, there is no accuracy loss with the graded mesh. The advantages of this element are demonstrated by analyzing the problem shown in Figure 2-13. In comparison the cost and the memory requirements vary as $\log_2 n$ for the graded mesh. The larger the problem is the greater the advantage of the graded mesh. This clearly illustrates that the gains from better algorithms can easily outpace the gains from better computers.



(A)

(B)

Figure 2-13: A uniform mesh $n=4$ (A) and McDill's grading scheme for a cube of $n=4$ (B). The number of elements is equal to n^3 and $7\log_2 n + 1$. The computational cost varies as n^7 and $\log_2 n$ (Where: n is the number of elements along an edge in a uniform mesh and, m is the number of recursive subdivisions of the upper left hand cube. Note: the size of the element in the upper left front corner is the same when $n=2^m$).

The second major weapon in the battle to reduce computing costs is the use of improved solvers. The use of incomplete Choleski conjugate gradient (*ICCG*) solvers with element-by-element preconditioning, which have been developed for fluids problems by Glowinski [12] and for structural problems by Jennings and Ajiz [13], has produced dramatic gains. These solvers do not factorize the global stiffness matrix completely.. Although the experience to date does not permit a definitive statement, Hughes [14 and 15] has developed an iterative method that promises to solve the problem and reduces *CPU* costs. The transient temperature fields shown in Figure 2-14 and 2-17 were computed on a workstation with such a solver.

The thinner the wall, the smaller is the three dimensional area around the heat source. An example is shown in Figure 2-14.

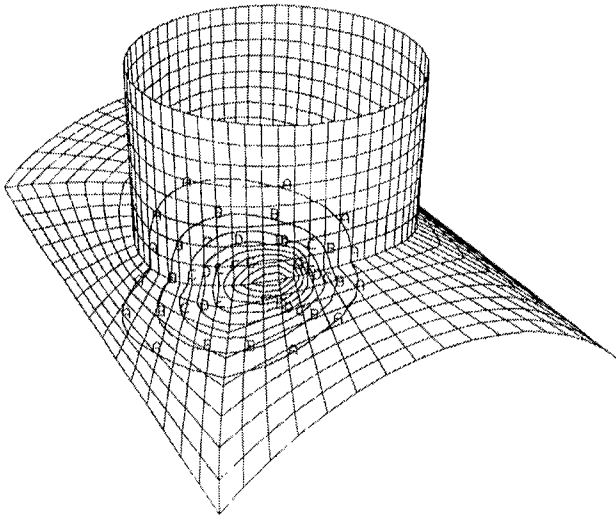


Figure 2-14: The contours of the transient temperature field are shown for a weld of a tee joint. The pipe is 40mm in diameter and the wall thickness is 2.5mm. Thermal shell elements are used to reduce the computing cost. The welding parameters are voltage 32, amperes 150, speed 1mm/s and power input 1.5 kJ/mm.

Since the 3D model is needed near the arc and the shell model is most efficient far from the arc, these models can be combined to produce a more efficient model. Figure 2-15 shows such a composite 3D-shell model. It requires a special transition element to join shell and 3D brick elements.

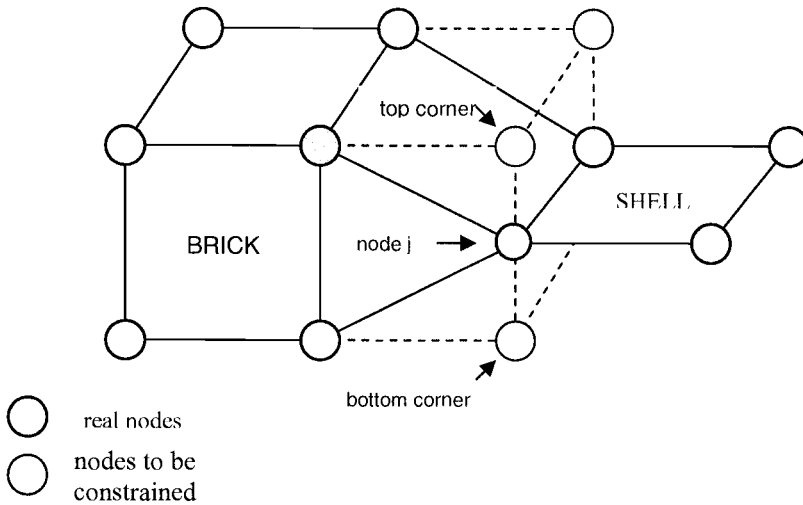


Figure 2-15: The transformation of a brick element to a transition element is shown. In particular, the relation between the transition node j and its top and bottom nodes is shown [67].

Gu in [67] presents a method to connect a three-dimensional element to the shell element. Figure 2-15 shows brick and shell elements and the transformation of a brick element to a transition element. The element is called a Shell-Brick transition element. It is not really a new element but a brick with constraints according to the shell assumption. It has more flexibility and can be added to other *FEM* packages without altering the original code.

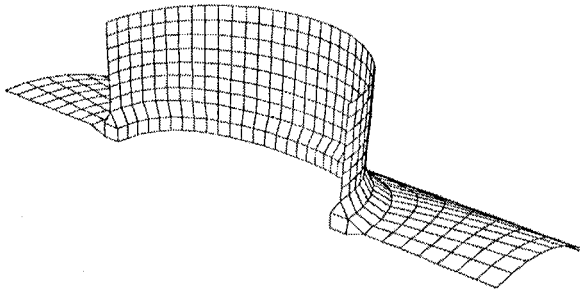


Figure 2-16: This tee joint is modeled with 4 noded thermal shell elements far from the weld joint, 8 noded 3D brick elements at the weld joint and special transition elements to join the shell and brick elements.

This composite kinematic model is more accurate than the shell mesh shown in Figure 2-16 and computationally cheaper than the mesh using 3D bricks shown in Figure 2-17.

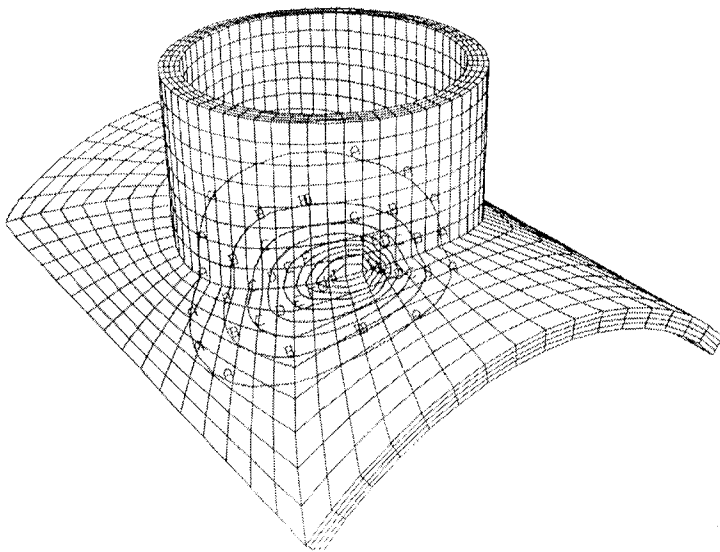


Figure 2-17: This tee joint is modeled with 8 noded 3D brick elements. This is the most accurate and the most expensive kinematic model.

The fundamental limitations of the most popular commercial mesh generators are that the mesh is difficult to change during an analysis; the mesh design requires expert judgment and it is labor intensive. Kela [7] and Sheperd and Law [8] developed a class of mesh generators which do not depend on expert judgment. They are fully automatic. Since as much as 90% of the time and cost of a Finite Element Method (*FEM*) analysis of a complex structure can be absorbed by pre and post processing, progress in mesh generation is a critical factor that is pacing the development of computational weld mechanics. Automatic mesh generators open the possibility of changing the mesh at any, even every, time step. This is particularly important in welding where a fine mesh is needed near the molten pool and a coarse mesh far from the molten pool could decrease costs and improve performance by several orders of magnitude. The arbitrary Euler-Lagrange method [9] would allow a fine mesh that

moves with the arc. The mesh far from the arc could be stationary. The mesh in between could move with a velocity that is interpolated.

The above examples suggest that rapid improvements in mesh generation methods that will reduce the cost of finite element analysis (*FEA*) of welds and permit real welding situations to be analyzed routinely. Many manufacturing processes are three-dimensional, nonlinear, transient processes in which the area of computational interest changes with time. Automatic finite element analysis AFEA with adaptive and dynamic mesh management has the potential to reduce substantially the cost of analysis for problems of this type.

In transient heat transfer analysis, the Finite Element Method (*FEM*) program must integrate a set of ordinary differential equations in time. Current commercial *FEM* programs use two point integration schemes that are either explicit or implicit. Explicit schemes use primarily element level operations. The cost per time step is small but time steps must be short because the element with the smallest critical time controls the time step. Implicit schemes solve a global set of linear equations. Each time step is more expensive but the time steps can be larger. Provided the load does not vary too rapidly in time, the longer time steps can be more efficient.

A recent development in integration schemes allows those elements with short critical time steps to be integrated implicitly with longer time steps and those elements with longer critical time steps to be integrated explicitly [17]. This can reduce computing costs significantly.

The generalization of this concept to use different time steps in different elements is called subcycling [16]. The mesh shown in Figure 2-18A is created by recursively subdividing the square m times.

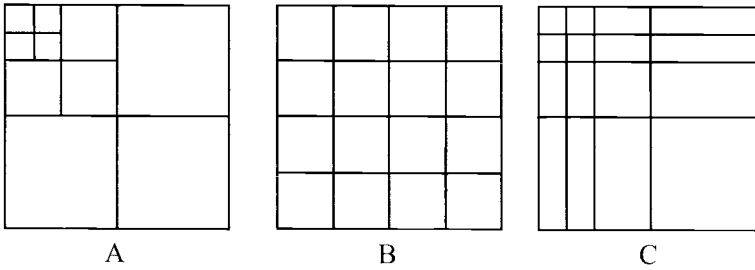


Figure 2-18: The mesh in (A) is obtained by recursively subdividing the square in the upper left hand corner. This can be significantly more efficient than the regular mesh shown in (B) or the grading strategy used in (C) for point like loads at the upper hand corner.

The number of elements is $1+3m$; the smallest element has edge length $L/2^m$ and critical time step $2^{2m}/\alpha L^2$. If each element is integrated only with its critical time step, the number of element time steps is $3(2^m - 1)$ or $O(2^m)$. If all elements are integrated with the smallest critical time step as is the current commercial practice, the number of element time steps is: $(1+3m)2^{2m}\alpha/L^2$ or $O(m2^{2m})$.

2.2.4 Evaluation of the Double Ellipsoid Model

In order to minimize the computing cost the initial analysis was done in the plane normal to the welding direction as shown in figures 2-19 and 2-20. Thus, heat flow in the welding direction was neglected. The above simplification is accurate in situations where comparatively little heat flows from the arc in the welding direction. This is reasonable when the arc speed is high. An estimate of the effect of this approximation has been given by Andersson [41] who argues that the errors introduced by neglecting heat flow in the direction of the moving electrode are not large, except in the immediate vicinity of the electrode.

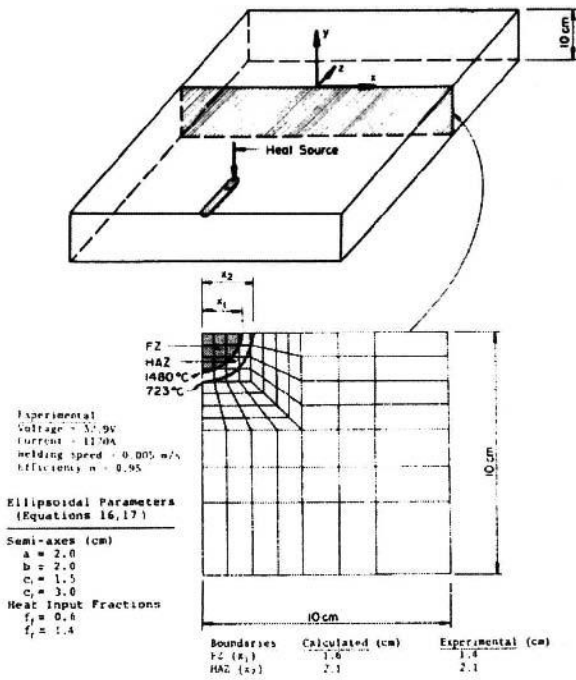


Figure 2-19: Experimental arrangement and FEM mesh for the thick section bead on plate weld [48 and 46].

In order to demonstrate the flexibility and assess the validity of the double ellipsoidal heat source model two quite different welding situations were considered.

The first case analyzed was a thick section (10cm) submerged arc bead-on-plate (low carbon structural steel) weld shown schematically in Figure 2-19. The welding conditions are also contained in the Figure.

Christensen [48] reported a 800 to 500 °C cooling time of 37 seconds for this weld and the FZ and HAZ sizes shown in the diagram. Shown also in the figure is the FEM mesh used to calculate these quantities. It is two-dimensional in x and y as previously explained. The temperature distribution in the ‘cross-section analyzed’ is calculated for a series of time steps as the heat source passes. In this way the FZ and HAZ cross-sectional sizes can be

determined, and from the time step-temperature data the cooling time 800 to 500 °C is calculated.

The second welding situation is taken from the work of Chong [49], Figure 2-20.

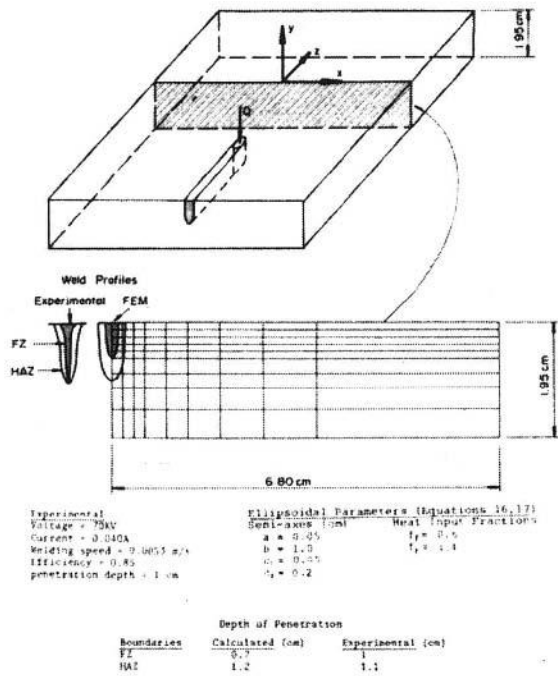


Figure 2-20: Experimental arrangement and FEM mesh for the deep penetration weld [46 and 49].

It is a partial penetration electron beam bead-on-plate (low carbon steel) weld. Traditionally the Rosenthal 2D model would be used to analyze this weld. However, there is some heat flow through the thickness dimension since the penetration is partial and, of course, the idealized line heat source is suspect. The ellipsoidal model can be easily adapted to this weld geometry by selecting appropriate characteristic ellipsoidal parameters. A cooling time (800 °C to 500 °C) of 1.9 seconds was measured by Chong [49] and the FZ and HAZ dimensions were reported [46].

In previous works the thermal properties and boundary conditions were usually set equal to a constant value. Convection and radiation are mostly ignored. The point, line and plane sources [37, 38 and 39]

idealize a heat source which in reality is distributed. These solutions are most accurate far from the heat source. At the source, the error in temperature is large, usually infinite. Near the heat source the accuracy can be improved by matching the theoretical solution to experimental data. This is usually done by choosing a fictitious thermal conductivity value.

With numerical methods, these deficiencies have been corrected and more realistic models that are just as rigorous mathematically have been developed. Perhaps the most important factor is to distribute the heat rather than assume point or line sources. Temperature dependent thermal conductivity and heat capacity can be taken into account, Figures 2-21 and 2-22. In addition, temperature dependent convection and radiation coefficients can be applied to the boundaries. For the radiation and convection boundary conditions, a combined heat transfer coefficient was calculated from the relationship:

$$H = 24.1 \times 10^{-4} \epsilon T^{1.61} \quad (2-18)$$

where ϵ is the emissivity or degree of blackness of the surface of the body. A value of 0.9 was assumed for ϵ , as recommended for hot rolled steel [37].

Contact thermal resistance between the plate and the jigging can be incorporated.

Bisra [50] and Mills [52] also present thermo-physical properties for selected commercial alloys. The thermal conductivity of steels at room temperature is reduced by increasing the amount of alloy substances, Figure 2-21. This situation is limited to the phase change temperature $A1$, from where the variation disappears in the slight rise of the curve.

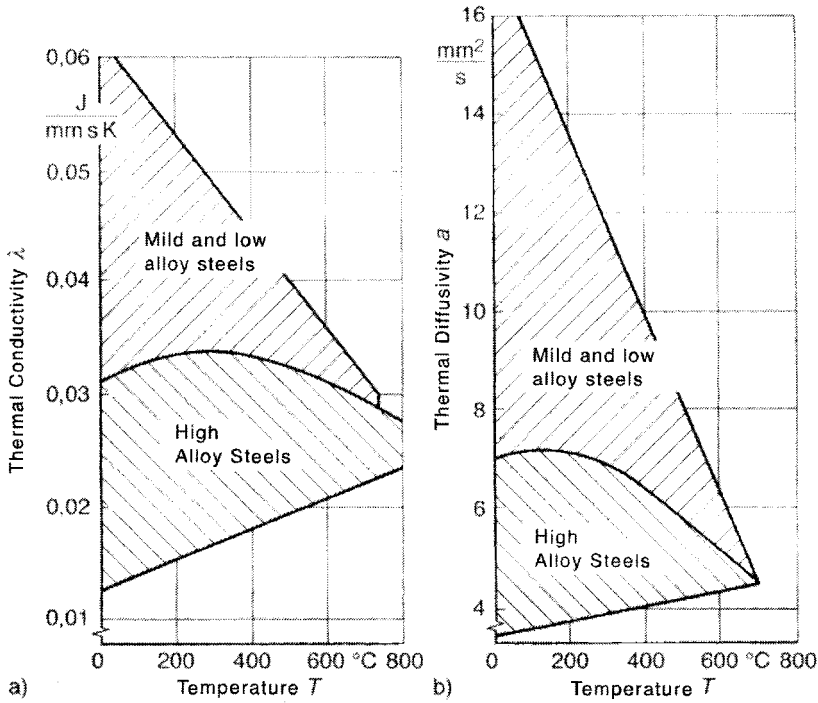


Figure 2-21: Thermal conductivity (a) and Thermal diffusivity (b) of steels as function of temperature; from [71 and 3].

The specific heat capacity for some steels as a function of temperature is shown in Figure 2-22.

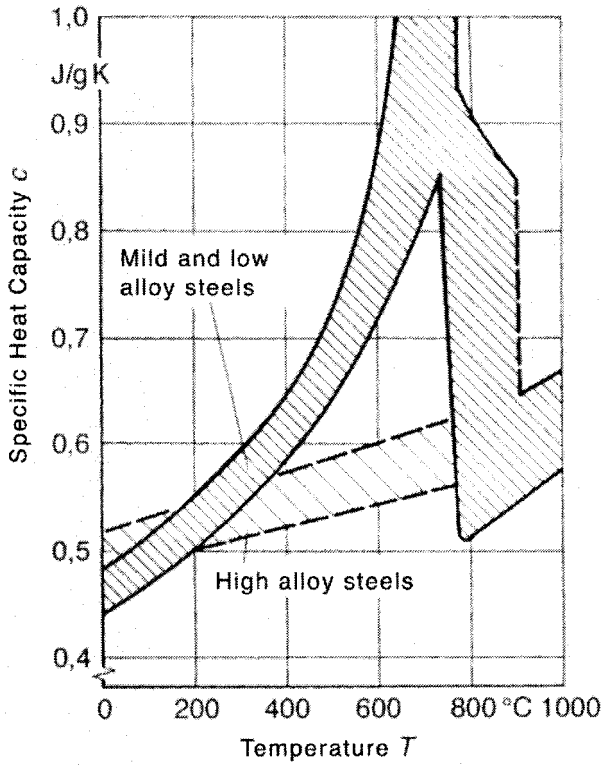


Figure 2-22: Specific heat capacity for some steels as function of temperature, latent heat at phase change temperature for ferrite pearlite (A1) and at phase change temperature for ferrite austenite (A3); from [71 and 3].

Figure 2-23 shows the density for some steels as a function of temperature.

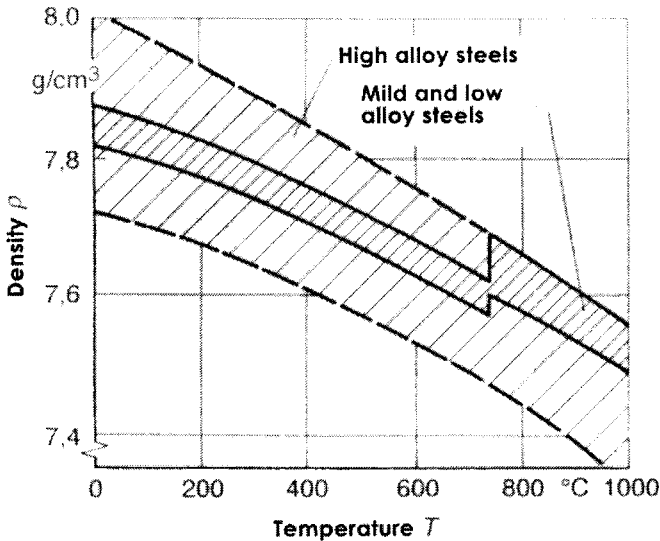


Figure 2-23: Density of some steels as function of temperature; from [71 and 3].

As shown in Figure 2-9 there are four characteristic length parameters that must be determined. Physically these parameters are the radial dimensions of the molten zone in front, behind, to the side and underneath the arc. If the cross-section of the molten zone is known from experiment, these data may be used to fix the heat source dimensions. For example, the width and depth are taken directly from a cross-section of the weld. In the absence of better data, experience suggests it is reasonable to take the distance in front of the heat source equal to one-half the weld width and the distance behind the heat source equal to twice the width. If cross-sectional dimensions are not available Christensen's expressions [48] can be used to estimate these parameters. Basically Christensen defines a non-dimensional operating parameter and non-dimensional coordinate systems. Using these expressions, the weld pool dimensions can be estimated.

The non-dimensional Christensen method was used to fix the ellipsoidal flux distribution parameters for the thick section bead on plate weld shown in Figure 2-19. The cross-sectional dimensions were reported by Chong, and the half-width dimension was applied to the flux distance in front of the electron beam heat source while

the twice-width distance was applied behind the *EB*. The heat input fractions used in the computations were based on a parametric study of the model. Values of $f_f = 0.6$ and $f_r = 1.4$ were found to provide the best correspondence between the measured and calculated thermal history results.

The temperature distribution along the width perpendicular to the weld center line at 11.5 seconds after the arc passed is shown in Figure 2-24 [46]. It is compared to the experimental data from Christensen et al. [48] and the finite element analysis of the same problem by Krutz and Segerlind [42] where a disc-shaped heat source (Eq. 2-4) was used. As expected, the ellipsoidal model gives better agreement with experiment than the disc.

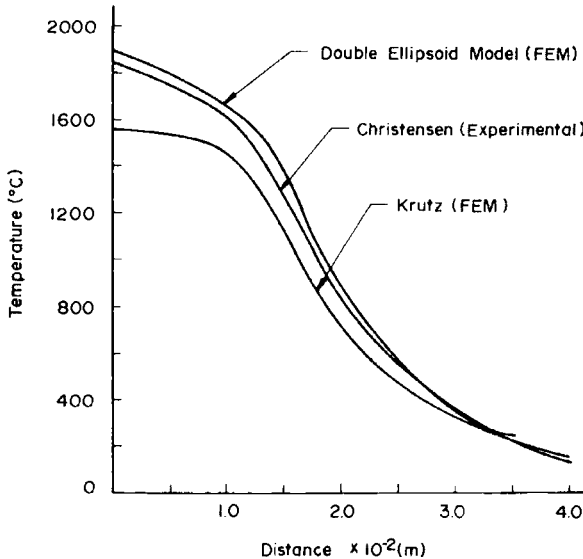


Figure 2-24: Temperature distribution along the top of the workpiece perpendicular to the weld. Experimental results of Christensen [48] compared to the computed values of Krutz and Segerlind 'disc model' [42] and the computed values using the 'double ellipsoid model' [46].

The fusion and heat affected zone boundary positions predicted by these *FEM* calculations, [46], are in good agreement with the experimental data, as shown in Figure 2-16. In addition, the *FEM* cooling times (800 °C to 500 °C) are much closer to the

experimental value than the cooling time calculated by the Rosenthal's analysis. The *FEM* cooling time is slightly larger than the experimental value. This may be due to neglecting the longitudinal heat flow. The radiation-convection applied to the top surface had little effect on the thermal cycle or the *FZ-HAZ* boundaries. This is to be expected for thick section welds where the heat flow is dominated by conduction.

A plot of the heat input at the surface using the double ellipsoid heat source is given in Figure 2-25, from Lindgren [22].

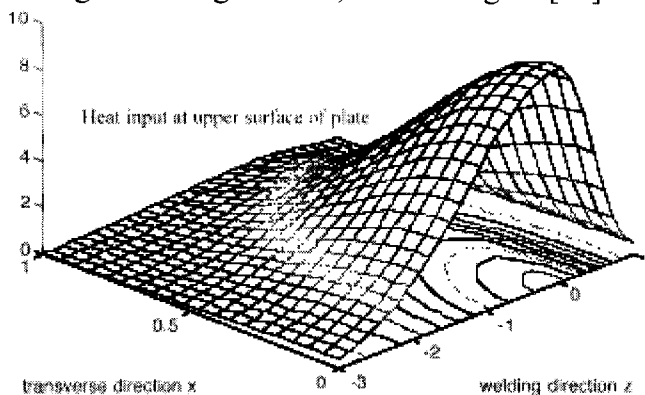


Figure 2-25: Heat input distribution using a double-ellipsoid heat source model, [22].

2.2.5 Modeling Thermal Stresses and Distortions in Welds

The thermal stress analysis of welds is more complex than the heat flow analysis because of the geometry changes and because of the complex stress-strain relationship. In designing a welding procedure, the critical issues are defects, mechanical properties, distortion and residual stress. Modeling stresses in welds includes all distortions that can be predicted by thermal stress analysis. Models of the mechanical properties of base metal, *HAZ* and weld metal, are needed as input data for thermal analysis. To evaluate the significance of a given defect, stress analysis is required.

Most thermal stress analyses have used thermo-elasto-plastic constitutive models with rate independent plasticity. Rate independent plasticity implies the viscosity is zero and therefore the

relaxation time is zero. This means the stress relaxes instantly to the yield stress. The higher the temperature and the longer the time, the more important viscous deformation becomes. A rate independent model is certainly not valid in the liquid region and is suspect near the melting point where viscous effects are expected to be important; most analyses assume a cutoff temperature. They assume that the thermal strain, Young's modulus and yield strength do not change above a cutoff temperature. Temperatures above this cutoff temperature are set to the cutoff temperature for the thermal stress analysis. For steels the cutoff temperatures which have been used range from 600-800 °C to 1100-1200 °C.

The analysis of stress and distortion in welds involves both rate dependent plasticity and rate independent plasticity. Plastic deformation below half the melting point temperature (measured in degree Kelvin) is usually rate independent plasticity. Stress relaxation by creep or by visco-plasticity is rate dependent plasticity and it should be considered for deformation above half the melting point, in multi-pass welds and in stress-relief of welds. Rate independent plasticity is independent of the deformation rate and therefore of time (in limited deformation rates or the ratio of deformation time to the active plastic deformation). The related characteristic behaviour in a simple one dimensional model is shown in Figure 2-26a.

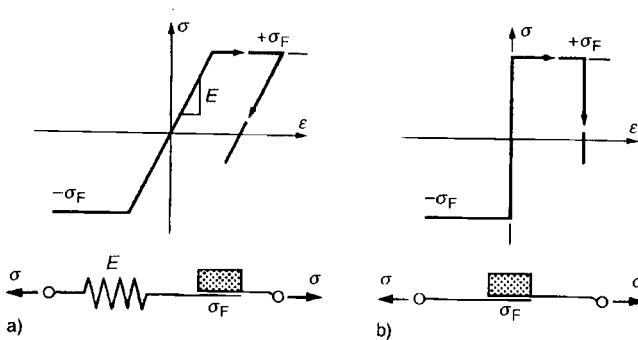


Figure 2-26a, b: One dimensional model of rate independent elasto-plastic a) and ideal plastic b) of material behaviour; Young's Modulus E , with yield strength σ_F ; with stress σ and strain ϵ , [3].

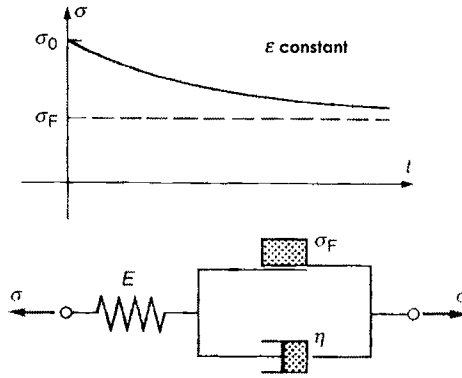


Figure 2-26c: One dimensional model of rate-dependent elasto-visco-plastic material behaviour; relaxation of beginning stress σ_0 by constant strain ϵ as a function of time t ; Young's Modulus E , with yield strength σ_F , dynamic viscosity η , [3].

To complete this, Figure 2-26b shows an ideal plastic model which is unsuitable for the evaluation of welding stress. In contrast to this, the elasto-visco-plastic continuum defines a plastic behaviour dependent on the deformation rate and therefore on time. The related characteristic behaviour in a simple one dimensional model and the relaxation behaviour are illustrated in Figure 2-27.

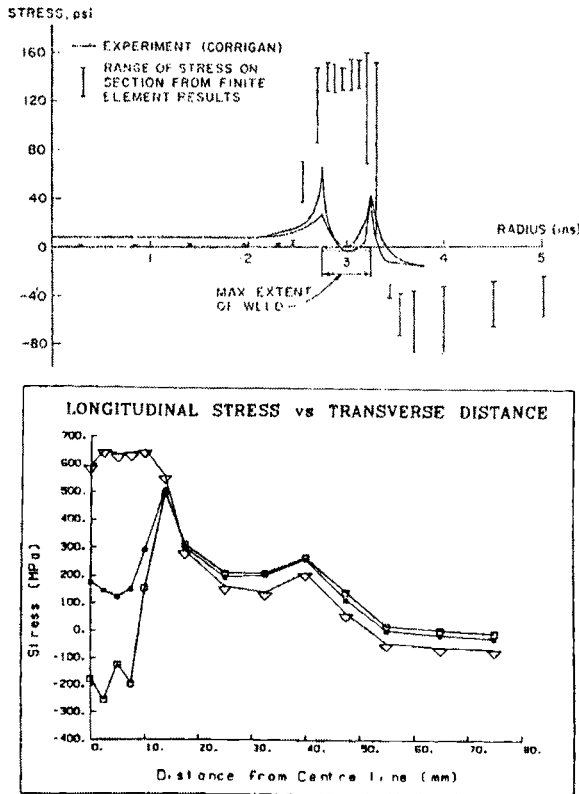


Figure 2-27: Residual longitudinal stress on the top surface vs. transverse distance from the weld centerline in HY-130 weld measured by Corrigan and computed by Hibbitt & Marcal [29] are shown in a). Note the lack of agreement between computed and measured stresses. The longitudinal stress shown in b) was computed by Oddy et al. [60] for HY-80 for three cases. The top curve ignores the phase transformation. The bottom curve includes the volume change due to the transformation. The middle curve includes the effect of transformation plasticity (In steel welds during the austenite-ferrite phase transformation the variations of stress and strain on the length scale of microstructure produce an important contribution to the plastic strain called transformation plasticity). Note the good agreement between experiment and the computed results for the middle curve.

Although the accuracy is limited by computational costs to rather coarse meshes, Figure 2-13, the residual stresses have usually agreed well with experimental results. An important exception has been the predicted residual stress in high strength steels. Hibbitt and Marcal

[29] attempted to predict the residual stress in welding *HY-130* steel. Their results were so different from experiment that they concluded that an important physical phenomenon had been missed, Figure 2-27.

In 1988, Oddy A. et al. [60] repeated the analysis but included the effect of the austenite to martensite transformation. They obtained the correct residual stress and showed that the critical phenomenon missed by Hibbitt and Marcal was transformation plasticity. This is the plastic strain that occurs during a phase change in the presence of a deviatoric stress.

Transient *3D* thermal stress analyses of welds have been described in detail in several papers [53, 56 and 65]. The thermal strain rate due to the transient temperature field induces an elastic, plastic and transformation plasticity strain rate. An exact solution to a stress analysis problem satisfies three basic laws; the conservation of linear momentum or the equilibrium equation, the constitutive relation between stress and strain and the compatibility relations between strain and displacements which is the conservation of mass. In addition it satisfies two types of boundary conditions; the prescribed displacements or essential boundary conditions and the prescribed tractions or natural boundary conditions. A displacement *FEM* formulation is used to solve the constitutive, compatibility and equilibrium equations. The displacements, rotations and strains are large, transient and *3D*. The thermal strain must be modeled with care (Oddy et al [65]) to avoid an incompatibility between thermal strain and strain from the displacement field.

Residual stress and distortion of welds are strong functions of plasticity. We are more concerned with the neighborhood of arc welds that have a small pool of liquid metal as distinct from the structure being welded.

Near the weld pool the kinematics is definitely *3D*. Farther from the weld pool, the kinematics in appropriate structures sometimes can be modeled with plane or shell models. The plane strain model was often used in the past, because it is computationally cheap.

During a phase transformation, the volume change induces a local variation in the stress field. For example, during the austenite to martensite transformation, the volume change could place a

martensite grain in compression and some of the surrounding austenite in tension just at its yield stress. If an average tensile stress is superimposed upon this microscopic stress field, the austenite could now yield in tension with an infinitesimal applied tensile stress. Now reverse the order. Apply an infinitely small macroscopic tensile stress first. Then transform some austenite to martensite to reach the yield stress of austenite locally. An additional transformation will cause plastic strain. This additional plastic strain is defined to be transformation plastic strain. It will stop when the transformation stops. It arises from the interaction between the microscopic and macroscopic stress fields. This two-scale or multi-scale is a bit similar to turbulence models in fluid flow that also use an average or macroscopic velocity and velocity fluctuation. If the macroscopic stress field is not modeled (i.e., the microscopic stress field is modeled directly), then classical plastic strain describes the deformation, and transformation plasticity does not occur. While the classical plastic strain rate is proportional to the deviatoric stress rate, the transformation plasticity strain rate is proportional to the product of the deviatoric stress times the transformation rate of the phase change. It is not creep because it is not proportional to time. Leblond's exposition of this theory is beautiful [57].

The high temperature range ($T \geq 0.5T_m$) is usually considered to be of minor importance in generating residual stress due to the low value of yield stress. However it is important in hot cracking that is caused by the high temperature strain close to the molten temperature. The geometric changes at high temperatures are inherited by regions that cool from high temperatures. These geometric changes can be very important. The thermo-mechanics of causing the residual stress by welding is shown schematically in Figure 2-28. In this figure the scheme of plastic zone distribution for a case of quasi-stationary temperature field caused by a moving line heat source is presented. The parabola-like curve drawn as a broken line separates the region being heated in front of the curve and the region being cooled behind the curve. The region being heated tends to be in compression and the region being cooled tends to be in tension. The elastic unloading zone shown as a strip separates the compressed and tensioned areas. For different points in the area the

schematics highlight the strain-stress cycle related to the local load cycle, without considering temperature dependency.

As an example, adopted from Pilipenko [18], the point 6 in Figure 2-28 may be suggested. At first sight the schematic stress-strain cycle in point 6 should have looked like point 5. But the difference is that material in point 6, after reaching some elastic and plastic compression, was ‘annealed’ inside of the material softening isotherm. Points 1, 2 and 3 represent the evolution of stress developed at a point lying at some distance from the weld centreline. First the material is being exposed to elastic compression (point 1), and then, reaching the yield limit, the material undergoes plastic deformation (point 2), followed by elastic unloading (point 3). Point 7 has a peculiar position. It lies on the weld centreline and the material in this point has been subjected only to elastic and then plastic tensioning.

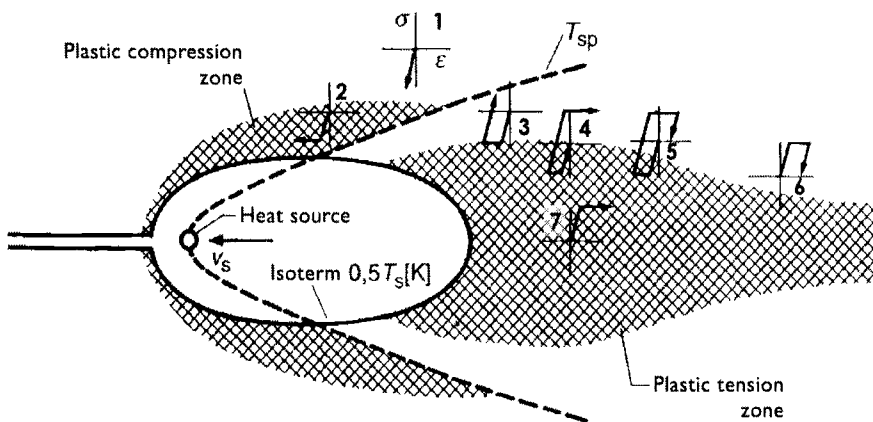


Figure 2-28: Plastic compression and tension zones; local stress-strain cycles in quasi-stationary temperature field of the moving heat source, from Radaj [3].

The temperature of the metal in welds varies from the boiling temperature to room temperature. The domain includes the liquid weld pool and the far field of solid near room temperature. The liquid is well described as a Newtonian fluid characterized by a temperature dependent viscosity. The temperature of the solid can be considered to be a linear viscous material characterized by a

viscosity due to the diffusion of dislocations. From temperatures above $T_{vp} \approx 0.5 \text{ or } 0.8 T_m$, the solid can be considered to be viscoplastic and characterized by an elasticity tensor, viscosity and deformation resistance. Below T_{vp} , the solid can be considered to be a rate independent plastic material characterized by an elasticity tensor, yield strength and isotropic hardening modulus. Thus the constitutive equation of a material point must be able to change type with space and time during the welding process. The constitutive model is assigned to be rate independent if the temperature is less than T_{vp} , rate dependent if the temperature is in a range $0.5\text{-}0.8 T_m$ and linear viscous if the temperature is greater than $0.8 T_m$, where T_m is a melting point or solidus temperature in degrees of Kelvin. The constitutive model type changes as a function of temperature in space and time.

The practical application of a weld simulation with different constitutive equations within the above mentioned temperature areas will be discussed in detail in chapter V.

An example of computed displacements in a weld is shown in Figure 2-29.

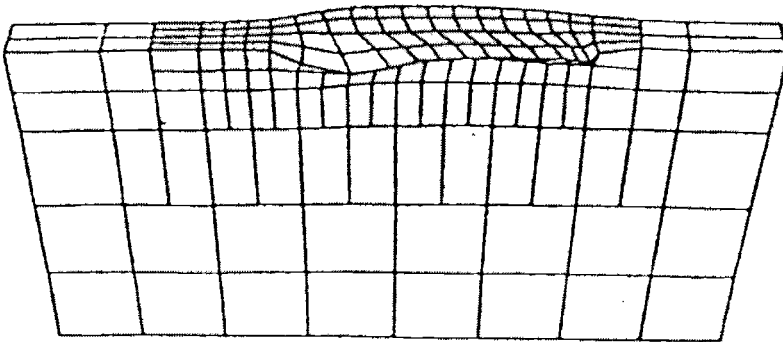


Figure 2-29: Displacements computed by a thermo-elasto-plastic analysis for a 1.6 kJ/mm edge weld on a carbon steel bar 12.7mm in width. Note that the displacements have been magnified by a factor of 50 to make them discernable. Note the displacements in the longitudinal direction that violate the assumptions of plane strain.

2.2.6 Microstructure Modeling in Heat Affected Zone (HAZ)

Many failures of welds initiate in the heat affected zone adjacent to the weld metal, e.g., in the coarse grained *HAZ*. For this reason, welding engineers devote much of their effort to controlling the microstructure and hence toughness of the *HAZ*. Metallurgists usually describe the evolution of microstructure in low alloy steels with isothermal transformation diagrams or continuous cooling transformation (*CCT*) diagrams. These diagrams are maps that depict the starting time and temperature of the various microstructural transformations that occur over a range of cooling trajectories. These diagrams have been developed for heat treating. Heat treating usually assumes an equilibrium microstructure at a soaking temperature of the order of 900 °C. The Jominy test, that imposes a jet of cold water on one end of a bar, is a physical model of the evolution of microstructure in heat treating.

This *CCT* model cannot be applied directly to welding for several reasons. The peak temperature in the *HAZ* of welds ranges from a bit below the eutectoid temperature to the melting point. Grain growth in the austensite phase is non-uniform in the *HAZ*. It is sensitive to the time and temperature curve and the presence of precipitates such as *NbC* that inhibit grain growth. Also the *CCT* diagrams are not a convenient representation for a computational model.

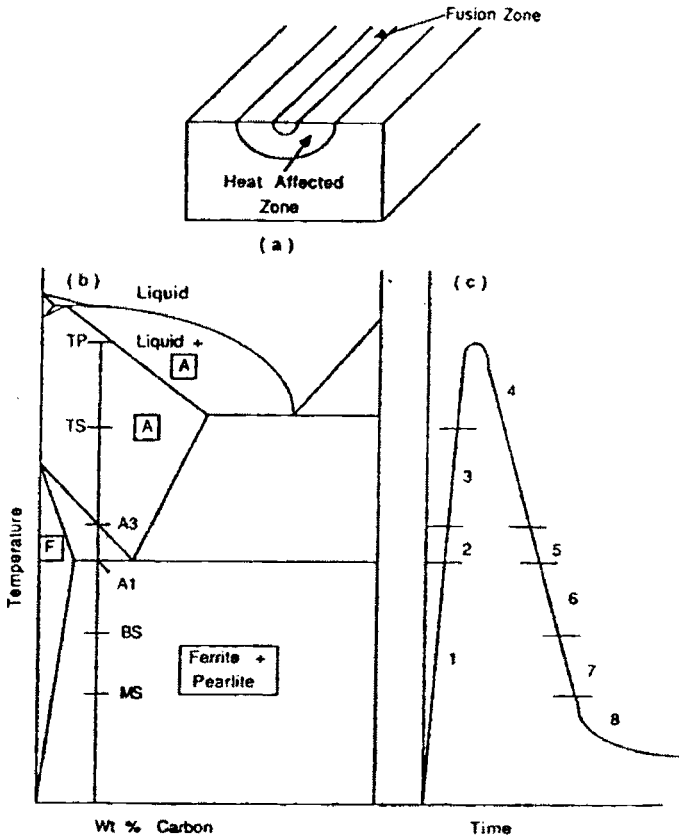


Figure 2-30: The microstructure at a point in the HAZ shown in a) under goes the thermal cycle shown in c). The microstructure evolves through the following stages: 1) ferrite and pearlite are at equilibrium; 2) ferrite and pearlite transform to austenite; 3) austenite grain growth is inhibited by NbC and VC; 4) austenite grain growth occurs; 5) austenite decomposes to ferrite; 6) austenite decomposes to pearlite; 7) austenite decomposes to bainite; 8) austenite decomposes to martensite.

For these reasons, the model developed by Kirkaldy et al.[61] for Jominy bars, was extended by Watt et al.[66] and Henwood et al.[62] to model the *HAZ* of welds in low alloy steels. Input data to this model are the composition of base metal, initial microstructure and the transient temperature computed from *FEM*. The output is the fraction of ferrite, pearlite, austenite, bainite, martensite and the grain size of the austenite at each point (x,y,z,t) .

The model begins by computing the *Fe-C* equilibrium diagram for this composition, Figure 2-30b.

For each time step in the transient analysis, the phase fractions at the start are initial data and the phase fractions at the end of the step are computed. On heating, phase transformations are assumed to occur so quickly that the kinetic effects can be ignored, i.e., local equilibrium is assumed. In effect, superheating is ignored. After ferrite and pearlite have fully transformed to austenite, austenite grain growth begins after the dissolution of *NbC* and/or *VC* if they are present. Austenite grain growth is evaluated by integrating an ordinary differential equation (*ODE*). Grain growth continues until the *A3* temperature is reached on cooling. At this time the decomposition of austenite to a) ferrite, b) pearlite and c) bainite is modeled with a sequence of *ODEs*. Finally, if austenite is still present at the martensite start temperature, austenite is transformed to martensite by an algebraic equation proposed by Koisten and Marburger [63].

The *ODE* for austenite to ferrite is shown in equation (2-19.):

$$\frac{dX}{dt} = \frac{2^{\frac{G-1}{2}} (\Delta T)^3 \exp\left(-\frac{23500}{RT}\right)}{59.6Mn + 1.45Ni + 67.7Cr + 24.4Mo} X^{\frac{2(1-X)}{3}} (1-X)^{\frac{2X}{3}} \quad (2-19)$$

The exponent containing *G*, the austenite grain size, in the first term reflects the fact that since ferrite nucleates at the austenite grain boundary, the density of nuclei is a function of the austenite grain boundary area. The next term reflects the metal physics experiments that shows the rate of growth of ferrite increases as ΔT^3 where $\Delta T = A3 - T$ is the undercooling temperature for the austenite-ferrite transformation. This is due to the increasing difference in free energy between austenite and ferrite with under-cooling. The exponential term reflects the decrease in the diffusivity of carbon in iron with temperature. The denominator reflects the effect of alloying elements on diffusivity. The last term is the predator prey factor which states that the rate of production of ferrite is a product of the fraction of ferrite present, *X*, and the fraction of austenite present (1-*X*).

$$X = \frac{X_F}{X_{FE}} \quad (2-20)$$

where X_F is the fraction of ferrite formed and X_{FE} is the equilibrium amount of ferrite.

$$G = 1 + 1.44 \left[\ln \left(\left(\frac{25.4}{g} \right)^2 \times 100 \right) \right] \quad (2-21)$$

where g is the grain size in microns.

Kirkaldy has proposed the following *ODE* relation for the austenite decomposition to pearlite and it is similar to equation (4-21):

$$\frac{dX}{dt} = \frac{2^{\frac{(G-1)}{2}} (\Delta T)^3 D}{1.79 + 5.42(Cr + Mo + 4MoNi)} X^{\frac{2(1-X)}{3}} (1-X)^{\frac{2X}{3}} \quad (2-22)$$

where ΔT is the undercooling given as $(A_1 - T)$ and D is a diffusion parameter and it is given by the following relation, adopted from [74]:

$$\frac{1}{D} = \frac{1}{\exp\left(-\frac{27500}{RT}\right)} + \frac{0.01Cr + 0.52Mo}{\exp\left(-\frac{3700}{RT}\right)} \quad (2-23)$$

and

$$X = \frac{X_P}{X_{PE}} \quad (2-24)$$

where X_P is the fraction of pearlite formed and X_{PE} is the equilibrium amount of pearlite. The equilibrium value of ferrite is calculated at each time step. Therefore the equilibrium amount of ferrite at any specific temperature is the maximum amount of ferrite which can be formed from austenite. The remaining amount of austenite is available for the formation of pearlite. This allows the value of X_{PE} to be set equal to $1 - X_{FE}$.

The *ODE* governing decomposition of austenite to bainite is taken from the work of Kirkaldy, adopted from Khoral [74]:

$$\frac{dX}{dt} = \frac{2^{\frac{(G-1)}{2}} (\Delta T)^2 \exp\left(-\frac{27500}{RT}\right)}{10^{-4}(2.34 + 10.1C + 3.8Cr + 19Mo)Z} X^{\frac{2(1-X)}{3}} (1-X)^{\frac{2X}{3}} \quad (2-25)$$

where X is the amount of bainite formed and ΔT is the undercooling given as $(BS-T)$. Z is given by the following relation:

$$Z = \exp[X^2(1.9C + 2.5Mn + 9Ni + 1.7Cr + 4Mo - 2.6)] \quad (2-26)$$

The value of Z is set to 1.0 if: $(1.9C + 2.5Mn + 9Ni + 1.7Cr + 4Mo - 2.6) < 0$.

The martensitic transformation is given by the following relation taken from the work of Koistinen and Marburger [63]:

$$X_M = 1 - \exp[-k_1(MS - T)] \quad (2-27)$$

where X_M is the volume fraction of martensite formed, MS is the martensite start temperature, T is the instantaneous temperature and k_1 is a constant and its value for most steel types is $0.011^\circ C^{-1}$.

This microstructure model does not apply to the weld metal because the effects of solidification are ignored. Bhadeshia [64] has developed models that could be applied to weld metal.

2.2.7 Spatial Integration Schemes

Since the Finite Element Method (*FEM*) is primarily an exercise in numerical integration, it is not surprising that better integration schemes are being sought. Numerical integration schemes replace an integral by a summation; e.g. $\int_{-1}^1 f(x)dx = \sum_{i=1}^n w_i f(x_i)$. The choice of the number of sampling points, i , the weights, w_i , and the location of the sampling points, x_i , characterize the integration scheme. If $f(x)$ is a polynomial of degree $2n-1$, it can be integrated exactly with n sampling or integration points as shown by Gauss. In two dimensions, the stiffness matrix of the popular 4 node rectangular element (but not a quadrilateral) can be integrated exactly with four integration points. If only one integration point is used, the integration is approximate and spurious nodes may appear that corrupt the solution. Belytschko [16] discovered a way to stabilize these spurious nodes and thus reduce the integration costs by almost a factor of four for 4-node quads and almost 8 for 8-node bricks.

References

1. Finger S. and Dixon J.R. A review of research in mechanical engineering design. Part I: descriptive, prescriptive and computer-based models of design process. *Research in Engineering Design*, 1989 1, pp 51-57
2. Finger S. and Dixon J.R. A review of research in mechanical engineering design. Part II: representation, analysis and design for the life cycle, *Research in Engineering Design*, No.1, p 121-137, 1989
3. Radaj D. Eigenspannungen und Verzug beim Schweißen, Rechen- und Messverfahren, Fachbuchreihe Schweißtechnik, DVS-Verlag GmbH, Duesseldorf 2000
4. Runnemalm H (1999). Efficient finite element modeling and simulation of welding. Doctoral Thesis, Lulea.
5. Chihoski Russel A. Understanding weld cracking in Aluminum sheet, *Welding Journal*, Vol. 25, pp 24-30, Jan. 1972
6. Requicha A.A.G. and Voelcker H.B. Solids modeling; current status and research directions, *IEEE Computer Graphics and Application*, Vol. 7, pp 25-37, 1983
7. Kela A., Voelcker H. and Goldak J.A. Automatic generation of finite element meshes from CSG representations of solids, International conference on accuracy estimates and adaptive refinements in finite element computations (ARFEC), sponsored by the International Association of Computational Mechanics, Lisbon Portugal June 19-20, 1984
8. Sheperd M.S. and Law K.H. The modified-quadtree mesh generator and adaptive analysis: International conference on accuracy estimates and refinements in finite element computations (ARFEC), sponsored by the International Association of Computational Mechanics, Lisbon Portugal, June 19-20, 1984
9. Donnea J. Arbitrary Lagrangian-Eulerian finite element methods, *Computational Methods for Transient Analysis*, vol. 1, North-Holland publishing Co, Edited by Belyschko T. and Hughes T.J.R., p 473-516, 1983
10. McDill JMJ, Goldak JA, Oddy AS, and Bibby MJ. Isoparametric quadrilaterals and hexahedrons for mesh-grading elements, *Comm. Applied Nu. Methods*, Vol. 3, pp 155-163, 1987
11. Swanson J.A., Cameron G.R. and Haberland J.C. Adapting the Ansys finite element program to an attached processor, *IEEE Computer Journal*, 1983, Vol. 16, No 6, pp 85-91
12. Glowinski R., Mantel B., Periaux J. Perrier P. and Pironneau: On an efficient new preconditioned conjugate gradient method. Application to the in-core solution of the Navier-Stokes equations via non-linear least-square and finite element methods, *Finite Elements in Fluids*, Vol. 4, pp 365-401, 1982
13. Ajiz M.A. and Jennings A. A robust incomplete choleski-cojugate gradient algorithm, *International Journal for Numerical Methods in Engineering*, Vol. 20, pp 949-966, 1984

14. Hughes T.J.R., Levit I. and Winget J. An element-by-element solution algorithm for problems of structural and solid mechanics, *Computer Methods in Applied Mechanics and Engineering*, Vol. 36, pp 241-254, 1983
15. Hughes T.J.R., Winget J., Levit I. and Tezduyar T.E. New alternative direction procedures in finite element analysis based upon EBE approximate factorizations, *ASME Proc. of Symp. On Recent Developments in Nonlinear Stress and Solid Mechanics*, June 1983
16. Belyschko T. An overview of semidiscretization and time integration procedures, *Computational Methods for Transient Solid Mechanics*, June 1983
17. Lui W.K. Mixed time integration methods for transient thermal analysis of structures, *Nasa Contractor Report 172209*, pp 1-55, Sept. 1983
18. Pilipenko A (2001) Computer simulation of residual stress and distortion of thick plates in multielectrode submerged arc welding. Doctoral thesis, Norwegian University of Science and Technology.
19. Mahin K.W., MacEwen S., Winters W. S., Mason W., Kanouff M. and Fuchs E.A. Evaluation of residual stress distortions in a traveling GTA weld using finite element and experimental techniques, *Proc. of Modeling of Casting and Welding Processes IV*, Ed. Giamei A.F. and Abbaschian G.R., pp 339-350, April 17-22, 1988, Pub. Eng. Foundation and TMS/AIME
20. Goldak J. A., Bibby M.J., Downey D. and Gu M. Heat and fluid flow in welds, *Advanced Joining Technologies*, *Proc. of the International Institute of Welding Congress on Joining Research*, July 1990
21. Tall L. Residual stresses in welded plates-a theoretical study, *Welding Journal*, Vol. 43, No. 1, pp 10s-23s, 1964
22. Lindgren L-E. Finite element modeling and simulation of welding Part I Increased complexity, *J of Thermal Stresses* 24, pp 141-192, 2001
23. Tsuji I. Transient and residual stresses due to butt-welding of mild steel plates, *Memoirs of the Faculty of Engineering, Kyushu University*, vol. XXVII, No. 3. 1967
24. Iwaki T. and Masubuchi K. Thermo-elastic analysis of orthotropic plastic by the finite element method, *J Soc. Naval Arch. Japan*, Vol. 130, pp 195-204, 1971
25. Ueda Y. and Yamakawa T. Thermal stress analysis of metals with temperature dependent mechanical properties, *Proc. int. Conf. Mech. Behavior of Materials*, p 10, 1971
26. Ueda Y. and Yamakawa T. Analysis of thermal elastic-plastic stress and strain during welding by finite element method, *JWRI*, Vol. 2, No. 2, pp 90-100, 1971
27. Ueda Y. and Yamakawa T. Mechanical cracking characteristics of cracking of welded joints, *Proc. of 1st Int. Symposium on Precaution of Cracking in Welded Structures Based on Recent Theoretical and practical Knowledge*, The Japan Welding Society, Tokyo Japan, p IC5.1, 1971

28. Fujita Y., Takesshi Y., Kitamura M. and Nomoto T. Welding stresses with special reference to cracking, IIW Doc X-655-72, 1972
29. Hibbitt H.D. and Marcal P.V. A numerical thermo-mechanical model for the welding and subsequent loading of a fabricated structure, *Computers & Structures*, Vol. 3, pp 1145-1174, 1973
30. Friedman E. Thermomechanical analysis of the welding process using the finite element method, *ASME J. Pressure Vessel Technology*, Vol. 97, No. 3, pp 206-213, Aug. 1975
31. Fujita Y., Takeshi Y. and Nomoto T. Studies on restraint intensity of welding, IIW Doc X-573-70, 1970
32. Fujita Y. and Nomoto T. : Studies on thermal stresses with special reference to weld cracking, 1st Int. Symposium on Precaution of Cracking in Welded Structures Based on recent Theoretical and Practical Knowledge, The Japan Welding Society, p IC6.1, 1971
33. Mahin K., Shapiro A.B., Hallquist J. Assessment of boundary conditions limitations on the development of a general computer Model for fusion welding , *Proc. of an International Conf. on Trends in Welding Technology*, pp 215-224, Gatlinburg Tennessee USA, May 18-22, 1986, ed. David S. A.
34. Tekriwal P., Mazumder J. Finite element modeling of the arc welding process, *Proc. of an international Conf. on Trends in Welding Technology*, pp 71-80, Gatlinburg Tennessee USA, May 18-22, 1986, ed. David S. A.
35. Goldak JA, McDill JMJ, Oddy AS, House R, Chi X and Bibby MJ. Computational heat transfer for Weld Mechanics, *Proc. of an International Conf. on Trends in Welding Technology*, pp 15-20, Gatlinburg Tennessee USA, May 18-22, 1986, ed. David S. A.
36. Goldak J. A., Patel B., Bibby M.J. and Moore J.E. Computational weld mechanics, Invited opening paper for AGARD Workshop-Structures and Materials 61st Panel Meeting, Oberammergau, Germany, pp 1-1 1-32, Sep. 8-13, 1985
37. Rykalin R.R. Energy sources for welding, *Welding in the World*, Vol. 12, No. 9/10, p 227-248, 1974
38. Rosenthal D.: the theory of moving sources of heat and its application to metal treatments, *Trans ASME*, Vol. 68, p 849-865, 1946
39. Myers P.O., Ueyhara O.A. and Borman G.L. Fundamentals of heat flow in welding, *Welding Research Council Bulletin*, New York No. 123, 1967
40. Pavelic V., Tanbakuchi R., Ueyhara O. A. and Myers: Experimental and computed temperature histories in gas tungsten arc welding of thin plates, *Welding Journal Research Supplement*, Vol. 48, pp 295s-305s, 1969
41. Andersson B.A.B. Thermal stresses in submerged-arc welded joint considering phase transformation, *Journal of Engineering Materials and Technology*, *Trans. ASME*, Vol. 100, pp 356-362, 1978
42. Krutz G.W. and Segerlind L.J. Finite element analysis of welded structures, *Welding Journal Research Supplement*, Vol. 57, pp 211s- 216s, 1978

43. Friedman E. Thermo-mechanical analysis of the welding process using the finite element method, *Journal Pressure Vessel Technology*, Trans. ASME, Vol. 97, No 3, pp 206-213, 1975
44. Paley Z. and Hibbert P.D. Computation of temperatures in actual weld designs, *Welding Journal Research Supplement*, Vol. 54, pp 385s-392s, 1975
45. Westby O. Temperature distribution in the workpiece by welding, Department of Metallurgy and Metals Working, The Technical University, Trondheim Norway, 1968
46. Goldak J., Chakravarti A. and Bibby M. A finite element model for welding heat sources, *Metallurgical Transactions B*, Vol. 15B, pp 299-305, June 1984
47. McDill JM, Oddy AS. and Goldak JA. An adaptive mesh-management algorithm for three-dimensional automatic finite element analysis, *Transactions of CSME*, Vol. 15, No 1, pp 57-69, 1991
48. Christensen N., Davies L.de.V. and Gjermundsen: *British Welding Journal*, Vol. 12, pp 54-75, 1965
49. Chong L.M. (1982). Predicting weld hardness. Master's Thesis, Carleton University.
50. The British Iron and Steel Research Association, *Physical Constants of Some Commercial Steels at Elevated Temperatures*, London Butterworths Scientific Publications, 1953
51. Ohji T. Physics of welding (1)- Heat conduction theory and its application to welding. *Welding Intern.* 8 (1994) 12, 938-942 trans. From *J Japan Welding Soc.* 63 (1994) 4, 32-36
52. Mills Kenneth C. Recommended values of thermo physical properties for selected commercial alloys, Woodhead Publishing Ltd ISBN 1 85573 569 5, ASM International ISBN 0-87170-753-5, 2002
53. Goldak J.A., Breiguine V., Dai N., Hughes E. and Zhou J. Thermal Stress Analysis in Solids Near the Liquid Region in Welds. *Mathematical Modeling of Weld Phenomena*, 3 Ed. By Cerjak H., The Institute of Materials, pp 543-570, 1997
54. Goldak J.A. et al. Coupling heat transfer, microstructure evolution and thermal stress analysis in weld mechanics. *IUTAM Symposium*, Lulea Sweden, 1991
55. Weber G. and Anand L. Finite deformation constitutive equations and a time integration procedure for isotropic, hyperelastic-viscoplastic solids, *Comput. Methods Appl. Mech. Eng.*, Vol. 79, pp 173-202, 1990
56. Oddy AS, Goldak JA and McDill MJ. Numerical analysis of transformation plasticity relation in 3D finite element analysis of welds, *European Journal of Mechanics, A/Solids*, Vol. 9, No. 3 pp 253-263, 1990
57. Leblond J.B., Mottet G. and Devaux J.C. A theoretical and numerical approach to the plastic behavior of steels during phase transformation-II, Study of classical plasticity for ideal-plastic phases, *J. Mech. Phys. Solids*, Vol. 34, pp 411-432, 1986

58. Gu M. and Goldak J.A. Steady state formulation for stress and distortion of welds, *J. of Eng. For Industry*, Vol. 116, pp 467-474, Nov. 1994
59. Goldak J. Keynote address modeling thermal stresses and distortions in welds, *Recent Trends in Welding Science and Technology TWR,89*, Proc. of the 2nd International Conference on Trends in welding Research, Gatlinburg Tennessee USA, 14-18 May 1989
60. Oddy A. Goldak J.A. and McDill J.M.J. Transformation effects in the 3D finite element analysis of welds, Proc. of the 2nd International Conf. on trends in Welding research, Gatlinburg Tennessee USA, May 1989
61. Kirkaldy J.S. and Venugopalan: In phase transformations in ferrous alloys, ed. By Marder A.R. and Goldenstein J.I., AM. Inst. Min. Engrs., Philadelphia, Pa, pp 125-148, 1984
62. Henwood C. Bibby M.J., Goldak J.A. and Watt D.F. Coupled transient heat transfer microstructure weld computations, *Acta Metal*, Vol. 36, No. 11, pp 3037-3046, 1988
63. Koisten D.P. and Marburger R.E. A general equation prescribing the extent of the austenite-martensite transformation in pure iron-carbon alloys and plain carbon steels, *Acta Met.*, Vol. 7, pp 59, 1959
64. Bhadeshia H. Modeling the microstructure in the fusion zone of steel weld deposits, *Proceedings of an International Conference on Trends in Welding Technology*, Gatlinburg Tennessee USA, ed. David S. A., May 15-19, 1989
65. Oddy A.S., McDill J.M. and Goldak J.A. Consistent strain fields in 3D finite element analysis of welds, *J. Pressure Vessel Tech.*, Vol. 25, No 1, pp 51-53, 1990
66. Watt D. F., Coon L., Bibby M. J., Goldak J.A. and Henwood C. Modeling microstructural development in weld heat affected zones, *Acta Metal*, Vol. 36, no 11, pp 3029-3035, 1988
67. Gu M. (1992). Computational weld analysis for long welds. Doctoral thesis Carleton University.
68. Bibby M.J., Shing G.Y. and Goldak J.A. A model for predicting the fusion and heat affected zone sizes of deep penetration welds, *CIM Metallurgical Quarterly*, Vol. 24, No. 2, 1985
69. Chakravarti A.P., Goldak J.A. and Rao A.S. Thermal analysis of welds, *International Conference on Numerical Methods in Thermal Problems*, Swansea UK, July 1985
70. Key J.F., Smartt H.B., Chan J.W. and McIlwain M. E. Process parameter effects on the arc physics and heat flow in GTAW, p 179-199
71. Richter F. Die wichtigsten physikalischen Eigenschaften von 52 Eisenwerkstoffen. *Stahleisen-Sonderberichte* No. 8, Publ. Stahleisen, Duesseldorf 1973
72. Sudnik W.A. and Erofeev W.A. Rastschety swarotschnych processov na iwm *Techn. Univ. Tula*, Sweden, 1986

73. Ohji T. Ohkubo A. and Nishiguchi K. Mathematical modeling of molten pool in arc welding, *Mechanical Effects of Welding*, p 207-214, Publ. Springer, Berlin 1992
74. Khoral P (1958) Coupling microstructure to heat transfer computation in weld analysis. Masters Thesis, Carleton University.
75. Okerblom, N.O. The calculations of deformations of welded metal structures, London, Her Majesty's Stationary Office, 1958
76. Vinokurov, V. A. Welding stresses and distortion, The British Library Board, 1977



<http://www.springer.com/978-0-387-23287-4>

Computational Welding Mechanics

Goldak, J.A.; Akhlaghi, M.

2005, XII, 322 p., Hardcover

ISBN: 978-0-387-23287-4